LOCAL BENCHMARKS FOR THE EVOLUTION OF MAJOR-MERGER GALAXIES—*SPITZER* OBSERVATIONS OF A *K*-BAND SELECTED SAMPLE

2010 ApJ 713 330

(http://iopscience.iop.org/0004-637X/713/1/330)

The Astrophysical Journal, 713:330–355, 2010 April 10 doi:10.1088/0004-637X/713/1/330

LOCAL BENCHMARKS FOR THE EVOLUTION OF MAJOR-MERGER GALAXIES—*SPITZER* OBSERVATIONS OF A *K*-BAND SELECTED SAMPLE

C. Kevin Xu[1], Donovan Domingue[2], Yi-Wen Cheng[1,3,4], Nanyao Lu[1], Jiasheng Huang[5], Yu Gao[6], Joseph M. Mazzarella[1], Roc Cutri[1], Wei-Hsin Sun[4], and Jason Surace[7]
[1] Infrared Processing and Analysis Center, California Institute of Technology 100-22, Pasadena, CA 91125, USA
[2] Georgia College & State University, CBX 82, Milledgeville, GA 31061, USA
[3] Institute of Astronomy, National Central University, Chung-Li 32054, Taiwan
[4] Institute of Astrophysics and Leung Center for Cosmology and Particle Astrophysics, National Taiwan University, Taipei 10617, Taiwan
[5] Harvard-Smithsonian Center for Astrophysics, 60 Garden Street, Cambridge, MA 02138, USA
[6] Purple Mountain Observatory, Chinese Academy of Sciences, 2 West Beijing Road, Nanjing 210008, China
[7] Spitzer Science Center, California Institute of Technology, Mail Stop 220-6, Pasadena, CA 91125, USA
Received 2009 September 14; accepted 2010 February 17; published 2010 March 22

ABSTRACT

We present *Spitzer* observations for a sample of close major-merger galaxy pairs (KPAIR sample) selected from cross-matches between the Two Micron All Sky Survey and Sloan Digital Sky Survey Data Release 3. The goals are to study the star formation activity in these galaxies and to set a local bench mark for the cosmic evolution of close major mergers. The *Spitzer* KPAIR sample (27 pairs, 54 galaxies) includes all spectroscopically confirmed spiral–spiral (S+S) and spiral–elliptical (S+E) pairs in a parent sample that is complete for primaries brighter than $K = 12.5$ mag, projected separations of $5\,h^{-1}$ kpc $\leqslant s \leqslant 20\ h^{-1}$ kpc, and mass ratios $\leqslant 2.5$. The *Spitzer* data, consisting of images in seven bands (3.6, 4.5, 5.8, 8, 24, 70, 160 μm), show very diversified IR emission properties. Compared to single spiral galaxies in a control sample, only spiral galaxies in S+S pairs show significantly enhanced specific star formation rate (sSFR = SFR/M), whereas spiral galaxies in S+E pairs do not. Furthermore, the SFR enhancement of spiral galaxies in S+S pairs is highly mass-dependent. Only those with $M \gtrsim 10^{10.5}\,M_{\odot}$ show significant enhancement. Relatively low-mass ($M \sim 10^{10}\,M_{\odot}$) spirals in S+S pairs have about the same SFR/M compared to their counterparts in the control sample, while those with $10^{11}\,M_{\odot}$ have on average a ∼3 times higher SFR/M than single spirals. There is evidence for a correlation between the global star formation activities (but not the nuclear activities) of the component galaxies in massive S+S major-merger pairs (the "Holmberg effect"). There is no significant difference in the SFR/M between the primaries and the secondaries, nor between spirals of SEP < 1 and those of SEP $\geqslant 1$, SEP being the normalized separation parameter. The contribution of KPAIR galaxies to the cosmic SFR density in the local universe is only 1.7%, and amounts to $\dot{\rho}_{\rm KPAIR} = 2.54 \times 10^{-4}\,(M_{\odot}\ {\rm yr}^{-1}\ {\rm Mpc}^{-3})$.

Key words: galaxies: evolution – galaxies: general – galaxies: interactions – galaxies: starburst

1. INTRODUCTION

Two questions about the evolution of galaxy mergers are being intensely debated in the current literature. (1) Does merger rate have a strong or weak cosmic evolution? (2) Are mergers responsible for the strong evolution of the cosmic star formation rate (SFR) since $z \sim 1$ (e.g., Lilly et al. 1996; Madau et al. 1998; Hopkins 2004)? Answers to these questions have important implications to the understanding of basic processes in galaxy formation/evolution, such as mass growth and star formation.

Earlier studies of merger rate, using samples of close galaxy pairs and morphologically disturbed systems in different redshift ranges, yielded a very broad range of the evolutionary index m, $m = 0$–6, assuming the evolution has a power-law form $(1+z)^m$ (Zepf & Koo 1989; Burkey et al. 1994; Carlberg et al. 1994; Yee & Ellington 1995; Woods et al. 1995; Patton et al. 1997; Wu & Keel 1998; Brinchmann et al. 1998; Le Févre et al. 2000; Carlberg et al. 2000; Patton et al. 2002; Conselice et al. 2003; Lin et al. 2004; Bundy et al. 2004; Lavery et al. 2004). More recent results can be divided into two camps, the "strong evolution" camp with $m \sim 3$ (Conselice 2006; Kampczyk et al. 2007; Kartaltepe et al. 2007) and the "weak evolution" camp with $m \sim 0.5$ (Lin et al. 2008; Lotz et al. 2008). The strong evolution scenario is consistent with the cosmic time dependence of the merging rate of dark matter halos (DMHs; Lacey & Cole 1993; Khochfar & Burkert 2001). However, more recent simulations including sub-halo structures support the weak evolution scenario (Berrier et al. 2006; Guo & White 2008).

Since the discovery of a strong evolution of the cosmic SFR (Lilly et al. 1996; Madau et al. 1998), many authors have argued that the primary cause is a rapid decline of merger-induced star formation (Driver et al. 1995; Glazebrook et al. 1995; Abraham et al. 1996; Brinchmann et al. 1998, Le Févre et al. 2000; Conselice et al. 2003). In particular, infrared (IR) surveys by both the *Infrared Space Observatory* (*ISO*; Elbaz et al. 2002) and *Spitzer* (Le Flóch et al. 2005) found that beyond $z \sim 0.7$–1.0, the cosmic star formation is contributed mostly by luminous IR galaxies (LIRGs) with $L_{\rm IR} \geqslant 10^{11}\,L_{\odot}$. In the local universe most LIRGs are in merger systems, and they contribute only a few percent of the integrated IR luminosity density (Sanders & Mirabel 1996). This seems to provide another argument for a strong evolution of merger-induced starbursts as the primary driver of the strong cosmic SFR evolution. However, are LIRGs at $z \sim 1$ indeed mostly in merger systems, as observed for their local counterparts? To this question, there are both positive answers (Zheng et al. 2004; Hammer et al. 2005; Bridge et al. 2007) and negative answers (Flores et al. 1999; Bell et al. 2005; Melbourne et al. 2005; Lotz et al. 2008). Authors in the latter group found that most LIRGs at $z \sim 1$ are normal late-type galaxies. According to them, it is the secular evolution of normal late-type galaxies that is mostly responsible for the cosmic SFR evolution, not the evolution of mergers.

What are the reasons for these controversies? Foremost among them are sample selection effects. There are two classical methods of selecting interacting/merging galaxies. One is to find galaxies with peculiar morphology (e.g., with tidal tails, double nuclei, or distorted disks) and the other is to identify paired galaxies. There are systematic differences between interacting galaxies selected using these two different methods. In the so-called merger sequence (Toomre 1977), galaxies in close pairs are usually mergers in the early stages when the two galaxies are still separable. In contrast, peculiar galaxies are mostly found in the later stages when the first collision between the two galaxies is happening or passed. However, this distinction is not clear-cut. Mergers such as the Antennae (= Arp 244) can be identified using both methods.

There are several known biases in the morphological selection method. The most serious one is due to the misidentifications of isolated irregular galaxies or starburst galaxies as mergers (Lotz et al. 2008). This effect is particularly severe for samples selected in the rest-frame UV bands (and to some extent those selected in the rest-frame B band), where the emission of young stars and dust extinction can significantly affect the surface brightness distribution. Another bias is caused by missing low surface brightness merger features, such as faint tidal tails and bridges, in observations that lack sufficient sensitivity. This incompleteness becomes increasingly severe for high-z surveys because of cosmic dimming.

The most common bias affecting current pair selected samples is an incompleteness known as "missing the secondary" (Xu et al. 2004). For flux-limited (= apparent magnitude limited) samples or luminosity limited (= absolute magnitude limited = "volume limited") samples, a paired galaxy brighter than the limit can be missed if its companion is fainter than the limit. The amplitude of this incompleteness can vary with the redshift, and cause significant bias in the results on the evolution of merger rate. For example, in many recent studies of merger rate evolution, pair fractions of galaxies of $M \leqslant M_{\rm lim}$ are compared, where $M_{\rm lim}$ is an absolute magnitude limit in the rest-frame B or V band. For these samples, the amplitude of the incompleteness due to the "missing the secondary" bias is on the order of $Q \sim 0.5\phi(M_{\rm lim})\delta M / \int_{-\rm inf}^{M_{\rm lim}} \phi(M)\, dM$, where ϕ is the luminosity function (LF) of the paired galaxies (e.g., Xu et al. 2004; Domingue et al. 2009), and δM is the typical magnitude difference between the two galaxies in a pair, which is $\sim$ 1 mag for major mergers. When $M_{\rm lim}$ is fixed, the ratio Q decreases with z if the LF has a positive "luminosity evolution" (i.e., the "knee" of the LF becomes brighter with increasing z), as observed for the LF of field galaxies (Wolf et al. 2003; Marchesini et al. 2007). This can introduce an artificial "evolution" of the merger rate in studies comparing pair fractions in samples at different redshifts that are limited by the same $M_{\rm lim}$ (e.g., Kartaltepe et al. 2007), and being responsible for the high evolutionary index ($m\sim$ 3) found in those studies. On the other hand, all studies in the "weak evolution" camp invoke a correction for the "passive luminosity evolution" (PLE), allowing the absolute value of $M_{\rm lim}$ to increase with z accordingly. This indeed reduces the effect of the incompleteness on the evolutionary index of the merger rate. However, as pointed out by Kartaltepe et al. (2007), there is no strong empirical justification for the PLE model. If the true evolution of the luminosities of interacting galaxies is different from PLE, then the bias is still present. It is better to get rid of the incompleteness from the merger rate studies in the first place.

Other biases for pair selections include: (1) contamination due to unphysical, projected pairs ("interlopers"), which affects mostly samples with incomplete redshifts or with only photometric redshifts; and (2) incompleteness due to missing of pairs in which the two galaxies are too close to be separated visually because of insufficient angular resolution or obscuration by dust.

Being aware of the selection effects that lead to the conflicting results, we set out to design a set of merger selection criteria that minimize the biases mentioned above. First, we opted for the pair selection method instead of the morphological selection method because, based purely on galaxy separation, pair selections are more objective. However, this also confines our study to systems prior to the final stages of the merging process. Second, we chose the rest-frame K as the wave band in which our samples are to be selected. This is the band least affected by star formation and dust extinction and most closely related to mass (Bell & De Jong 2001). Third, we confine ourselves to close major-merger pairs with mass ratio < 2.5 and with projected separation in the range $5\ h^{-1}$ kpc $\leqslant s \leqslant 20\ h^{-1}$ kpc ($h = H_0/(100\ {\rm km\ s^{-1}\ Mpc^{-1}})$). Many studies have found that only major mergers with separations comparable to the size of galaxies (i.e., $\lesssim 20\ h^{-1}$ kpc) show significant SFR enhancements (Xu & Sulentic 1991; Barton et al. 2000; Lambas et al. 2003; Nikolic et al. 2004; Alonso et al. 2004; Woods et al. 2006; Barton et al. 2007; Ellison et al. 2008). Other detailed selection criteria are presented in Section 2. It should be emphasized that, when studying the evolution of interacting galaxies, samples at different redshifts must be selected using identical criteria.

In two earlier papers (Xu et al. 2004; Domingue et al. 2009), we started from samples in the local universe, with the goal of setting local benchmarks for merger rate evolution. Xu et al. (2004), using a sample of 19 close major-merger pairs selected from the matched Two Micron All Sky Survey (2MASS)/2dFGRS catalog (Cole et al. 2001), derived the K-band luminosity function (KLF) and the differential pair fraction function (DPFF) of local binary galaxies. This was followed up by a more extended analysis (Domingue et al. 2009), exploiting a large sample of 173 close major-merger pairs selected from 2MASS/SDSS-DR5 cross-matches. Assuming the mass-dependent merger timescale of Kitzbichler & White (2008), Domingue et al. (2009) found that the differential merger rate increases with mass, and the merger rate versus mass relation is in good agreement with what being found in the N-body simulations of Maller et al. (2006).

In this paper, we report *Spitzer* imaging observations (seven bands at 3.6, 4.5, 5.8, 8, 24, 70, and 160 μm) of 27 galaxy pairs in the local universe, selected from cross-matches of 2MASS and Sloan Digital Sky Survey Data Release 3 (SDSS-DR3). The scientific goals are (1) studying the star formation activity in these galaxies and (2) setting a local bench mark for the evolution of the SFR in close major mergers. Assuming that only late-type galaxies contribute significantly to the total SFR, our analysis is concentrated on spiral (S) galaxies in spiral–spiral (S+S) and spiral–elliptical (S+E) pairs. The main focus of this paper is on the enhancement (or the lack of it) of the SFR of paired galaxies. Most previous studies on this subject are based on optical/UV observations susceptible to dust extinction (Barton et al. 2000, 2007; Lambas et al. 2003; Nikolic et al. 2004; Alonso et al. 2004; Woods et al. 2006; Woods & Geller 2007; Ellison et al. 2008). Early FIR studies based on *IRAS* observations (Kennicutt et al. 1987; Telesco et al. 1988; Xu &

Sulentic 1991) cannot resolve the pairs because of the coarse angular resolution of *IRAS*. The more recent *ISO* study of Xu et al. (2001) and *Spitzer* study of Smith et al. (2007), which resolved pairs into discrete regions (e.g., nuclei of component galaxies, bridges and tails, overlapping regions between the two disks, etc.), are confined to pairs with strong interacting features, and therefore are biased to interacting galaxies with strong star formation enhancement. This work shall be neutral to these biases. Our studies on IR spectral energy distributions (SEDs; D. L. Domingue et al. 2010, in preparation) and on the optical properties including new Hα and Hβ imaging observations (Y. W. Cheng et al. 2010, in preparation) will be published separately. Throughout this paper, we adopt the Λ-cosmology with $\Omega_m = 0.3$ and $\Omega_\Lambda = 0.7$, and $H_0 = 75$ (km s^{-1} Mpc^{-1}).

2. THE SAMPLE

The sample of galaxy pairs was selected from cross-matches between the 2MASS Extended Source Catalog (XSC; Jarrett et al. 2000) and the galaxy catalog of SDSS-DR3 (Abazajian et al. 2005). The selection procedure is similar to that in Xu et al. (2004) and Domingue et al. (2009). First, the following two criteria were set for galaxies to be considered in the pair selection.

1. Galaxies should be brighter than $K_s = 13.5$ mag, the completeness limit of the XSC (Jarrett et al. 2000). The default K_{20} magnitude is used for the K_s band (2.16 μm) fluxes (Jarrett et al. 2000). The K_{20} magnitudes were taken from Domingue et al. (2009), for which the photometric error due to the blending of close neighbors was corrected. As in Xu et al. (2004), a uniform -0.2 mag correction was applied to the K_{20} of galaxies when extrapolation to total K-band magnitude was necessary.
2. Galaxies should have the redshift completeness index c_z>0.5, where c_z is the ratio of the number of galaxies with measured redshifts within 1° radius from the center of the galaxy in question and the number of all galaxies within the same radius (Xu et al. 2004). This confines the pair selection to regions where the SDSS-DR3 has good spectroscopic coverage.

The resulting sample has 50,312 galaxies, of which 42,847 have measured redshifts (85% redshift completeness). A comparison with the number counts of 2MASS galaxies (Kochanek et al. 2001) yielded an equivalent sky coverage of $\Omega = 3000$ deg^2 ($\Omega = N/\mathrm{CN}$, where number counts CN is in units of deg^{-2}).

Pair selection was then carried out with the following criteria.

1. The K_s magnitude of the primary is brighter than 12.5 mag. A primary is defined as the brighter component of a pair.
2. The K_s difference between the two components is less than 1 mag: $\delta K_s \leqslant 1$ mag.
3. At least one of the components has spectroscopic redshift.
4. The projected separation is in the range of 5 h^{-1} kpc $\leqslant s \leqslant$ 20 h^{-1} kpc.
5. The velocity difference is less than 500 km s^{-1}: $\delta \mathrm{v} \leqslant$ 500 km s^{-1}.

Criteria 1 and 2 ensure that, by construction, all galaxies in this pair sample are brighter than $K_s = 13.5$, the completeness limit of the 2MASS survey (Jarrett et al. 2000). Therefore, the sample *does not* suffer from the "missing the secondary" bias that plagued many earlier merger studies (see Section 1). This also restricts our sample to major-merger pairs whose mass ratios are $\leqslant 2.5$. Criterion 4 makes the comparisons between local pairs in this sample and pairs in high-z samples robust. For high-z galaxies, it is difficult to distinguish a galaxy pair from a single galaxy if the separation is $\leqslant 5$ h^{-1} kpc, and the probability for chance pairs is significantly higher if projected separation is much larger than 20 h^{-1} kpc (Kartaltepe et al. 2007).

A total of 57 pairs were selected according to the criteria. Component galaxies are classified as either "S" or "E" using the following scheme: first, classical "eyeball" classifications were carried out. Independently, two of us (C.K.X. and D.D.) inspected the SDSS optical image of every galaxy in the sample and assigned a type to it according to its morphology. In addition, we also run an automatic classification script. It classifies a galaxy as "E" if $u - r > 2.22$ and $R_{50}/R_{90} < 0.35$, where R_{50} and R_{90} are the radii containing 50% and 90% of the Petrosian flux (Park & Choi 2005). Otherwise, the galaxy is classified as "S" type. The final classification is the median of the two eyeball results and the result of the automatic method. We excluded 20 pairs in which both components are "E" types ("E+E" pairs). According to their optical colors and EW(Hα), little star formation is evident, consistent with *IRAS* results on E+E pairs (Xu & Sulentic 1991). In order to minimize the contamination due to interlopers, single-redshift pairs were also excluded. We would stress that, judging from SDSS images, these single-redshift pairs do not show any special characteristics compared to the total sample, therefore dropping them will not introduce any significant bias to our study.

The final sample (KPAIR hereafter) for the *Spitzer* observations contains 27 S+S and S+E pairs. Among the 54 component galaxies, 42 are classified as S and 12 as E. They are listed in Table 1. The mass in the table (and hereafter) is the so-called stellar mass, excluding the mass of the dark matter and gas. It is estimated from the K-band luminosity by assuming a mass-to-luminosity ratio of 1.32 (solar units), taken from Cole et al. (2001) for the Salpeter initial mass function (IMF).[8] The heliocentric velocities are from SDSS-DR3, and the 60 μm flux densities are from the *IRAS* Faint Source Catalog (Moshir et al. 1992).

3. *SPITZER* OBSERVATIONS

IR imaging observations of all pairs but J1315+6207 in Table 1 were carried out in 2005 and 2006 under the Spitzer Cycle 2 GO Program "Local Benchmarks for the Evolution of Interacting Galaxies" (PID no. 20187). These include images in the four bands (3.6, 4.5, 5.8, and 8.0 μm) of the Infrared Array Camera (IRAC; Fazio et al. 2004) and in three bands (24, 70, and 160 μm) of the Multiband Imaging Photometer for Spitzer (MIPS; Rieke et al. 2004). KPAIR J1315+6207 (UGC08335a/b) is included in the Spitzer GO-1 survey of LIRGs (J. M. Mazzarella et al. 2010, in preparation). Its IRAC data were taken from J. M. Mazzarella et al. (2010, in preparation), while its MIPS observations were unsuccessful.

3.1. IRAC

3.1.1. Observations

All but three pairs in our sample are smaller than 2.′5 at optical wavelengths. Each pair (or each pair component for the three large pairs) was observed with the IRAC instrument in Full Array mode. High dynamic range settings and a 12

[8] The mass-to-luminosity ratio estimated using the Kennicutt IMF is a factor of 0.55 lower (Cole et al. 2001) and that estimated using the Kroupa IMF is a factor of 0.59 lower (Kauffmann et al. 2003).

Table 1
KPAIR Galaxy Sample

(1) Pair ID (KPAIR)	(2) Galaxy ID (2MASX)	(3) R.A. (J2000)	(4) Decl. (J2000)	(5) V_z (km s^{-1})	(6) K_s (mag)	(7) log(M) ($M_\odot$)	(8) Type	(9) $f_{60\,\mu m}$ (Jy)	(10) $L_{60\,\mu m}$ (log($L_\odot$))
J0020+0049	J00202580+0049350	00h20m25.8s	+00d49m35s	5078	10.99	10.84	S	0.62	9.68
	J00202748+0050009	00h20m27.5s	+00d50m01s	5480	10.50	11.04	E		
J0109+0020	J01093371+0020322	01h09m33.7s	+00d20m32s	13499	12.39	11.08	E		
	J01093517+0020132	01h09m35.1s	+00d20m13s	13319	12.47	11.05	S		
J0118−0013	J01183417−0013416	01h18m34.1s	−00d13m42s	14219	12.05	11.27	S 2	3.48	11.30
	J01183556−0013594	01h18m35.6s	−00d13m59s	14273	12.88	10.93	S		
J0211−0039	J02110638−0039191	02h11m06.3s	−00d39m21s	5920	11.42	10.77	S 2		
	J02110832−0039171	02h11m08.3s	−00d39m17s	6016	10.90	10.98	S		
J0906+5144	J09060283+5144411	09h06m02.8s	+51d44m41s	8849	11.68	11.01	E		
	J09060498+5144071	09h06m05.0s	+51d44m07s	8852	11.95	10.90	S 2		
J0937+0245	J09374413+0245394	09h37m44.1s	+02d45m39s	6988	10.01	11.46	S	2.00	10.43
	J09374506+0244504	09h37m45.0s	+02d44m50s	6790	10.45	11.29	E		
J0949+0037	J09494143+0037163	09h49m41.4s	+00d37m16s	1861	11.59	9.71	S	2.27	9.36
	J09495263+0037043	09h49m52.6s	+00d37m05s	1918	10.98	9.95	S		
J1020+4831	J10205188+4831096	10h20m51.9s	+48d31m10s	15886	13.26	10.88	S		
	J10205369+4831246	10h20m53.6s	+48d31m24s	15930	12.27	11.27	E R		
J1027+0114	J10272950+0114490	10h27m29.5s	+01d14m48s	6727	11.79	10.73	S		
	J10272970+0115170	10h27m29.7s	+01d15m16s	6661	10.90	11.08	E		
J1043+0645	J10435053+0645466	10h43m50.5s	+06d45m47s	8262	11.96	10.83	S		
	J10435268+0645256	10h43m52.7s	+06d45m25s	8088	12.20	10.73	S		
J1051+5101	J10514368+5101195	10h51m43.6s	+51d01m20s	7503	10.27	11.41	E	0.78	10.07
	J10514450+5101303	10h51m44.5s	+51d01m30s	7138	10.97	11.13	S		
J1202+5342	J12020424+5342317	12h02m04.3s	+53d42m32s	19366	12.97	11.16	S		
	J12020537+5342487	12h02m05.3s	+53d42m48s	19156	12.43	11.37	E		
J1308+0422	J13082737+0422125	13h08m27.4s	+04d22m13s	7186	13.39	10.15	S		
	J13082964+0422045	13h08m29.6s	+04d22m05s	7251	12.44	10.53	S		
J1332−0301	J13325525−0301347	13h32m55.3s	−03d01m35s	14297	12.95	10.90	S	0.57	10.51
	J13325655−0301395	13h32m56.6s	−03d01m40s	14000	12.19	11.21	S		
J1346−0325	J13462001−0325407	13h46m20.0s	−03d25m41s	6949	11.20	11.01	S		
	J13462215−0325057	13h46m22.2s	−03d25m06s	7171	11.66	10.82	E 2		
J1400+4251	J14005782+4251207	14h00m57.8s	+42d51m20s	9689	11.89	11.01	S	2.32	10.80
	J14005882+4250427	14h00m58.8s	+42d50m42s	9923	12.18	10.90	S		
J1425+0313	J14250552+0313590	14h25m05.5s	+03d13m59s	10693	11.98	11.06	E 1		
	J14250739+0313560	14h25m07.4s	+03d13m55s	10807	12.97	10.66	S		
J1433+4004	J14334683+4004512	14h33m46.8s	+40d04m52s	7674	10.78	11.25	S	1.80	10.48
	J14334840+4005392	14h33m48.4s	+40d05m39s	7788	11.17	11.10	S		
J1453+0317	J14530282+0317451	14h53m02.8s	+03d17m46s	1576	10.67	9.92	S	0.29	8.30
	J14530523+0319541	14h53m05.2s	+03d19m54s	1573	10.05	10.17	S		
J1506+0346	J15064391+0346364	15h06m43.9s	+03d46m36s	10498	11.48	11.22	S	0.27	9.91
	J15064579+0346214	15h06m45.8s	+03d46m22s	10183	11.61	11.17	S		
J1510+5810	J15101587+5810425	15h10m15.8s	+58d10m43s	9161	11.77	11.02	S	0.29	9.86
	J15101776+5810375	15h10m17.8s	+58d10m37s	9563	12.35	10.79	S		
J1528+4255	J15281276+4255474	15h28m12.8s	+42d55m48s	5588	10.02	11.26	S	1.10	9.96
	J15281667+4256384	15h28m16.6s	+42d56m39s	5345	10.59	11.03	S		
J1556+4757	J15562191+4757172	15h56m21.9s	+47d57m17s	5741	12.10	10.49	S	0.53	9.71
	J15562738+4757302	15h56m27.4s	+47d57m30s	5980	12.16	10.46	E		
J1602+4111	J16024254+4111499	16h02m42.6s	+41d11m50s	10019	11.69	11.11	S	1.43	10.60
	J16024475+4111589	16h02m44.7s	+41d11m59s	9950	12.50	10.78	S		
J1704+3448	J17045089+3448530	17h04m50.9s	+34d48m53s	17163	13.07	11.01	S	1.41	11.06
	J17045097+3449020	17h04m50.9s	+34d49m02s	16893	12.40	11.28	S		
J2047+0019	J20471908+0019150	20h47m19.1s	+00d19m15s	4209	9.08	11.37	S	0.34	9.18
	J20472428+0018030	20h47m24.3s	+00d18m03s	3795	9.74	11.10	E		
J1315+6207	J13153076+6207447	13h15m30.8s	+62d07m45s	9170	11.99	10.91	S	11.39	11.47
	J13153506+6207287	13h15m35.1s	+62d07m29s	9176	11.54	11.09	S		

Notes. Descriptions of columns: 1. Pair ID. The designations are "KPAIR J0020+0049," etc; 2. Galaxy ID, taken from 2MASS; 3. R.A. (J2000); 4. Decl. (J2000); 5. Recession velocity taken from SDSS; 6. K_s (K_{20}) magnitude taken from 2MASS; 7. Logarithm of the stellar mass of the galaxy; 8. Morphological type. Galaxies containing known active galactic nuclei (AGNs; via NED) are flagged with 1, 2, or *R* to indicate type 1, type 2, or radio AGNs; 9. The *IRAS* 60 μm flux density of the total pair; 10. The 60 μm luminosity (νL_ν) of the total pair.

position Reuleaux dither pattern were utilized. The dynamic range setting was designed to incorporate short exposures of 0.4 s along with longer exposures of 12 s, in order to acquire photometry on potentially saturated nuclei as well as reach the requested signal-to-noise ratio for the outer galaxy regions. The dither pattern produces the redundancy needed to eliminate

cosmic rays. The average surface brightness sensitivity levels (4σ) are 0.032, 0.048, 0.160, and 0.316 MJy sr^{-1} in the four IRAC bands, respectively.

3.1.2. Data Reduction

The Basic Calibrated Data (BCD) images were produced in the Spitzer Science Center (SSC) pipeline and these served as the start of our data reduction process. Custom IDL tools created by one of us (J.S. Huang of the IRAC instrument team) were used to apply the additional steps of pointing refinement, distortion correction, and mosaicking with sigma-clipping for the rejection of cosmic rays. The long and short exposures were processed independently for the purpose of creating mosaics in all four bands. These mosaics were resampled from the native 1.″22 pixel scale to a 0.″66 pixel scale.

Aperture photometry was carried out on the images in order to obtain flux densities in the four IRAC bands. Two different methods were applied to different sources:

1. Standard aperture photometry for individual galaxies. This was performed on well-separated pairs, utilizing both IPAC Skyview and IRAF APPHOT. Several blank sky regions were chosen from within the IRAC field containing the galaxy pairs. These regions were used to calculate the mean background value for subtraction. The standard deviation of their means provides estimate of the uncertainties of background subtraction (Smith et al. 2007). Apertures of different shapes (circular, eliptical, and polygon) are chosen according to the situation.
2. Aperture photometry first for the total pair and then for one of the components. This was performed on pairs whose two component galaxies are too close to be separated cleanly. We always chose the galaxy that has a more regular morphology (point-source-like or a regular elliptical) for the aperture photometry. This flux is then subtracted from the flux of the total pair, which yields the flux of the other component.

In addition to total fluxes of whole galaxies, circular aperture fluxes on two physical scales corresponding to $D = 4$ and 10 kpc, respectively, were also obtained. These fluxes sample the nucleus and disk emissions.

In the analysis of IRAC extended sources, it has been found that light is scattered out of the apertures into the array. The effect is most severe in the 5.8 and 8.0 μm channels. The SSC has developed "best practices" for applying aperture corrections. These corrections are dependent upon the IRAC channel and the area within the aperture (or "effective circular aperture radii"). All of the reported fluxes (Table 3) have this aperture correction applied, which introduces an uncertainty of $\sim$ 10% to the flux densities. No color correction is applied to the IRAC data.

The errors of the IRAC photometry are dominated by two uncertainties: for bright sources the uncertainty of the aperture correction is dominant, and for the faint sources the uncertainty of the background subtraction becomes important. The errors reported in Table 3 were determined as the quadratic sum of the two.

3.2. MIPS

3.2.1. Observations

The 24 μm observations used the small-field photometry mode. Both the 70 μm and the 160 μm observations used the 3×1 raster map mode, with a 1/8 array step size in the cross-scan direction. These provided images of $\sim 5'$ on one side and no less than 2.′5 on the other side, large enough to include some background regions for the sky subtraction, as well as to have the central $2.'5 \times 2.'5$ of each map to be fully sampled. For the three pairs larger than 2.′5, the same observation configuration was applied to each component instead of the total pair. For all fields, the same exposure time and same number of cycles were applied, which are ($t_{\rm exp}$ in s, $N_{\rm cycle}$) = (10, 1), (10, 1), and (10, 4) at 24, 70, and 160 μm, respectively. These corresponded to effective integration times of 165.7, 125, and 83.9 s for the three bands, and yielded average surface brightness rms noise (4σ) of 0.28, 2.0, and 6.0 MJy sr^{-1} in these bands, respectively.

3.2.2. Data Reduction

The BCD images were taken directly from the products of SSC pipeline (ver. 13). These are calibrated images of individual exposures (MIPS Data Handbook). The following major artifacts on the BCD images were corrected in our data reduction process:

1. "Stripes" in the 70 μm images. These are caused by flat-fielding variations due either to the latents of the stim flash or to the long term responsivity variation. All of our 70 μm observations were affected, some more severely than others. Following the recommendations in the MIPS Data Manual, we performed self-flat-fielding using our own data. This was done by calculating for each detector pixel the 2σ clipped median over all BCD frames within the given observation. Dividing the BCDs by the self-flat-field image removed the artificial stripes.
2. Dark latents in the 24 μm images. These are long timescale (up to 10 hr) artifacts produced by very bright sources. Two of our observations were affected: AORKEY=14271232 and AORKEY=14270720 (see Table 2). In both cases, the bright source which causes latents was not in the field of view. The same self-flat-fielding method for the correction of the artificial stripes in the 70 μm images was exploited in the correction for these artifacts.
3. Gradients in the 24 μm images. These non-astronomical gradients are due to poor flat fielding. If not corrected, they produce artificial discontinuities in the mosaicked images. Most of the 24 μm BCDs were affected by this. We fitted a slope to the sky background of each individual BCD and subtracted it. This effectively took out the gradients.

After these corrections, the SSC software MOPEX was used to make the mosaic image out of the BCD frames for each 24 μm or 70 μm MIPS observation. The 160 μm maps were taken from the post-BCD products of the same SSC pipeline. Combined mosaic images were produced using MOPEX for the three large pairs that have MIPS observations of the two components separately.

Flux densities of individual galaxies in pairs were measured from the corresponding images. Given the relatively large beams and small separations of pair components, it was challenging to carry out these measurements. Two different methods have been exploited:

1. *Aperture photometry*. When only one of the two components in a pair is detectable or, if both components are bright in the given MIPS band, the two components are separable, the flux densities were measured using aperture photometry. Polygon apertures were used in order to avoid overlapped apertures, with the aperture size changing with the galaxy size. The aperture corrections were estimated using two different methods. In all cases except for the

Table 2
The *Spitzer* Observations

			IRAC		MIPS		On-Source Time			
Pair ID (KPAIR)	R.A. (J2000)	Decl. (J2000)	AORKEY	ObsDate (yy/mm/dd)	AORKEY	ObsDate (yy/mm/dd)	IRAC (s)	24 μm (s)	70 μm (s)	160 μm (s)
(1)	(2)	(3)	(4)	(5)	(6)	(7)	(8)	(9)	(10)	(11)
J0020+0049	00h20m26.6	+00d49m48s	14276608	05/07/22	14269440	06/07/15	144.0	165.7	125.8	83.9
J0109+0020	01h09m34.4	+00d20m23s	14276864	06/01/01	14269696	06/07/19	144.0	165.7	125.8	83.9
J0118−0013	01h18m34.9	−00d13m51s	14277120	05/08/20	14269952	06/07/21	144.0	165.7	125.8	83.9
J0211−0039	02h11m07.3	−00d39m19s	14277376	05/08/21	14270208	06/02/14	144.0	165.7	125.8	83.9
J0906+5144	09h06m03.8	+51d44m24s	14277632	05/11/26	14270464	05/12/04	144.0	165.7	125.8	83.9
J0937+0245	09h37m44.6	+02d45m15s	14277888	05/11/26	14270720	05/12/03	144.0	165.7	125.8	83.9
J0949+0037A	09h49m52.6	+00d37m05s	14278144	05/12/27	14270976	05/12/03	144.0	165.7	125.8	83.9
J0949+0037B	09h49m41.4	+00d37m16s	14278400	05/12/27	14271232	05/12/03	144.0	165.7	125.8	83.9
J1020+4831	10h20m52.8	+48d31m17s	14278656	05/11/24	14271488	05/12/01	144.0	165.7	125.8	83.9
J1027+0114	10h27m29.5	+01d15m03s	14278912	05/12/24	14271744	06/06/07	144.0	165.7	125.8	83.9
J1043+0645	10h43m51.6	+06d45m36s	14279168	06/01/03	14272000	06/06/07	144.0	165.7	125.8	83.9
J1051+5101	10h51m44.2	+51d01m25s	14279424	05/11/24	14272256	05/12/05	144.0	165.7	125.8	83.9
J1202+5342	12h02m04.8	+53d42m40s	14279680	05/12/24	14272512	05/12/05	144.0	165.7	125.8	83.9
J1308+0422	13h08m28.6	+04d22m09s	14279936	05/07/24	14272768	06/02/21	144.0	165.7	125.8	83.9
J1332−0301	13h32m55.9	−03d01m37s	14280192	05/07/24	14273024	06/03/01	144.0	165.7	125.8	83.9
J1346−0325	13h46m21.1	−03d25m23s	14280448	05/07/24	14273280	06/03/01	144.0	165.7	125.8	83.9
J1400+4251	14h00m58.3	+42d51m02s	14280704	06/02/13	14273536	06/06/12	144.0	165.7	125.8	83.9
J1425+0313	14h25m06.5	+03d13m58s	14280960	05/07/24	14273792	06/03/01	144.0	165.7	125.8	83.9
J1433+4004	14h33m47.5	+40d05m15s	14281216	05/07/25	14274048	06/03/01	144.0	165.7	125.8	83.9
J1453+0317A	14h53m02.8	+03d17m46s	14281472	05/07/24	14274304	06/03/01	144.0	165.7	125.8	83.9
J1453+0317B	14h53m05.2	+03d19m54s	14281728	05/07/24	14274560	06/02/25	144.0	165.7	125.8	83.9
J1506+0346	15h06m44.9	+03d46m29s	14281984	05/07/24	14274816	06/03/01	144.0	165.7	125.8	83.9
J1510+5810	15h10m16.8	+58d10m40s	14282240	05/07/25	14275072	06/02/22	144.0	165.7	125.8	83.9
J1528+4255	15h28m14.6	+42d56m13s	14282496	05/07/24	14275328	06/03/03	144.0	165.7	125.8	83.9
J1556+4757	15h56m24.7	+47d57m24s	14282752	05/07/24	14275584	06/05/06	144.0	165.7	125.8	83.9
J1602+4111	16h02m43.7	+41d11m55s	14283008	05/07/24	14275840	05/08/29	144.0	165.7	125.8	83.9
J1704+3448	17h04m50.9	+34d48m58s	14283776	05/07/24	14284032	05/08/29	144.0	165.7	125.8	83.9
J2047+0019A	20h47m24.3	+00d18m03s	14283264	05/10/21	14276096	05/11/10	144.0	165.7	125.8	83.9
J2047+0019B	20h47m19.1	+00d19m15s	14283520	05/10/21	14276352	05/11/10	144.0	165.7	125.8	83.9

six 160 μm measurements in which the galaxy in question is extended in the 160 μm band, the aperture corrections were estimated under the point-source assumption, exploiting the point response function (PRF) presented in Appendix B. For the 24 μm and 70 μm sources that are significantly larger than a point source, this is an underestimation of the real aperture correction, though the fractional aperture correction itself decreases with source size. For the extended 160 μm sources, the aperture corrections were estimated differently. Because of the relatively small size of the 160 μm images compared to the beam, much of the emission of any galaxy that is extended in the 160 μm falls out of the 160 μm image, and would not be recovered if an aperture correction based on the point-source assumption were applied. In order to fully recover the missing flux, the following method was carried out. First, the 24 μm image (two times larger than the 160 μm image) was convolved with the PRF of the 160 μm band. Then, under the assumption that the f_{160}/f_{24} ratio is constant across the galaxy in question, the desired aperture correction in the 160 μm band was estimated from the ratio between the total flux in the 24 μm band and that in the 160 μm aperture measured on the smoothed 24 μm image. From experiments with individual sources, the following aperture-correction errors were assigned: 14% for weak sources in the 24 μm band, 5% for other 24 μm sources and all 70 μm sources, and 10% for all 160 μm sources.

2. *PRF fitting*. This was applied to pairs in which both component galaxies are detectable point sources and the two PRFs overlap with each other. In these cases, the flux densities of the two components were measured by simultaneously fitting two PRFs within a pair, positions and brightness of the two PRFs being the free parameters (altogether six of them: x_1, y_1, peak$_1$, x_2, y_2, peak$_2$). The average flux measurement errors are 14%, 5%, and 21% in the 24, 70, and 160 μm bands, respectively.

MIPS data are calibrated assuming a nominal spectrum of a blackbody at 10,000 K. This is very different from the dust emission in galaxies. Therefore color corrections, calculated using the modified blackbody spectra ($\beta = 2$) of temperatures of 100 K, 20 K, and 20 K, were applied to the 24 μm, 70 μm, and 160 μm band flux densities, respectively. The corresponding correction factors (multiplicative) are 0.967, 0.923, and 0.954.

The errors of the MIPS photometry are the quadratic sum of (in the order of importance): (1) the aperture-correction/model-fitting error (dominant for all sources except for the faintest ones), (2) the uncertainty of the background subtraction, and (3) the rms of the background. We ignored the photon noise which is never significant. The 4σ upper limits for the undetected sources were estimated using the quadratic sum of the uncertainty of the mean background value and the rms of the background. The apertures adopted in these estimates were derived from the *K*-band Kron radii taken from the 2MASS database. However, for a given MIPS band, if the Kron radius of a galaxy is less than a minimum value corresponds to the beam, then the aperture is derived using the minimum (8″, 20″, and 40″ for 24, 70, and 160 μm, respectively).

Table 3
IR Emission of Paired Galaxies

(1) Galaxy ID	(2) Aperture (kpc)	(3) $f_{3.6\,\mu m}$ (mJy)	(4) $f_{4.5\,\mu m}$ (mJy)	(5) $f_{5.8\,\mu m}$ (mJy)	(6) $f_{8\,\mu m}$ (mJy)	(7) $f_{24\,\mu m}$ (mJy)	(8) $f_{70\,\mu m}$ (mJy)	(9) $f_{160\,\mu m}$ (mJy)	(10) Photometry	(11) L_{TIR} ($L_\odot$)	(12) L_{IR} ($L_\odot$)
J00202580+0049350	4	6.20 ± 0.62	4.24 ± 0.42	10.05 ± 1.01	28.20 ± 2.82						
	10	10.66 ± 1.07	7.08 ± 0.71	11.85 ± 1.19	29.82 ± 2.99						
	Total	14.34 ± 1.44	9.26 ± 0.93	13.10 ± 1.35	30.84 ± 3.11	55.53 ± 2.87	677.27 ± 73.41	1375.07 ± 152.44	AAA	10.03	10.02
J00202748+0050009	4	10.56 ± 1.06	6.53 ± 0.65	4.48 ± 0.45	2.90 ± 0.29						
	10	16.25 ± 1.62	9.93 ± 0.99	6.65 ± 0.68	4.46 ± 0.48						
	Total	17.39 ± 1.74	10.61 ± 1.06	6.97 ± 0.74	4.78 ± 0.56	2.68 ± 0.15	<33.87	<101.60	AAA	< 8.96	9.01
J01093371+0020322	4	1.93 ± 0.19	1.24 ± 0.12	0.74 ± 0.07	0.45 ± 0.05						
	10	3.34 ± 0.33	2.15 ± 0.21	1.32 ± 0.13	0.88 ± 0.09						
	Total	3.97 ± 0.40	2.60 ± 0.26	1.46 ± 0.23	0.98 ± 0.21	<0.47	<10.57	<64.39	AAA	< 9.58	< 9.03
J01093517+0020132	4	1.27 ± 0.13	0.83 ± 0.08	0.52 ± 0.05	0.30 ± 0.03						
	10	2.65 ± 0.26	1.78 ± 0.18	1.17 ± 0.12	0.70 ± 0.07						
	Total	3.52 ± 0.35	2.36 ± 0.24	1.48 ± 0.21	0.86 ± 0.17	<1.03	<11.40	<91.13	AAA	< 9.58	< 8.99
J01183417−0013416	4	4.58 ± 0.46	3.99 ± 0.40	8.44 ± 0.84	33.48 ± 3.35						
	10	6.69 ± 0.67	5.87 ± 0.59	13.59 ± 1.36	56.31 ± 5.63						
	Total	7.46 ± 0.75	6.41 ± 0.64	14.17 ± 1.48	57.06 ± 5.71	249.73 ± 34.96	2817.82 ± 305.30	2749.61 ± 293.58	PPP	11.41	11.36
J01183556−0013594	4	0.51 ± 0.05	0.31 ± 0.03	0.43 ± 0.05	1.92 ± 0.19						
	10	1.86 ± 0.19	1.25 ± 0.13	2.18 ± 0.23	9.21 ± 0.92						
	Total	4.05 ± 0.41	2.83 ± 0.29	4.97 ± 0.87	20.20 ± 2.03	24.99 ± 3.50	305.32 ± 33.19	549.92 ± 73.94	PPP	10.55	10.67
J02110638−0039191	4	6.74 ± 0.67	4.95 ± 0.50	11.35 ± 1.14	30.82 ± 3.08						
	10	10.22 ± 1.02	7.32 ± 0.73	15.72 ± 1.61	42.62 ± 4.26						
	Total	11.62 ± 1.16	7.75 ± 0.78	16.17 ± 1.74	41.71 ± 4.17	75.18 ± 3.89	1034.44 ± 112.08	2184.97 ± 237.30	AAA	10.33	10.28
J02110832−0039171	4	8.28 ± 0.83	5.42 ± 0.54	3.82 ± 0.39	2.83 ± 0.28						
	10	12.81 ± 1.28	8.27 ± 0.83	5.90 ± 0.69	4.73 ± 0.48						
	Total	12.87 ± 1.29	8.29 ± 0.83	5.72 ± 0.71	4.32 ± 0.45	3.25 ± 0.17	<13.77	<102.84	AAA	< 9.36	9.13
J09060283+5144411	4	4.25 ± 0.42	2.78 ± 0.28	1.69 ± 0.17	1.07 ± 0.11						
	10	6.42 ± 0.64	4.31 ± 0.43	2.68 ± 0.31	1.78 ± 0.18						
	Total	7.97 ± 0.80	5.63 ± 0.57	3.61 ± 1.18	2.21 ± 0.36	0.69 ± 0.10	<6.89	<71.07	WAA	< 9.07	9.03
J09060498+5144071	4	1.80 ± 0.18	1.21 ± 0.12	1.05 ± 0.11	1.60 ± 0.16						
	10	4.26 ± 0.43	2.88 ± 0.29	3.07 ± 0.35	5.91 ± 0.59						
	Total	7.04 ± 0.71	4.80 ± 0.49	5.83 ± 0.94	13.10 ± 1.32	18.06 ± 0.93	191.21 ± 20.76	885.31 ± 93.44	AAA	10.17	10.08
J09374413+0245394	4	8.53 ± 0.85	5.70 ± 0.57	7.41 ± 0.74	20.82 ± 2.08						
	10	21.66 ± 2.17	15.26 ± 1.53	26.77 ± 2.71	75.67 ± 7.57						
	Total	21.66 ± 2.17	15.26 ± 1.53	26.77 ± 2.71	75.67 ± 7.57	183.80 ± 9.50	2133.90 ± 231.20	5989.62 ± 629.23	AAA	10.85	10.73
J09374506+0244504	4	11.42 ± 1.14	7.03 ± 0.70	4.60 ± 0.46	2.83 ± 0.28						
	10	17.38 ± 1.74	10.74 ± 1.07	7.03 ± 0.82	4.57 ± 0.48						
	Total	21.03 ± 2.10	12.90 ± 1.30	8.79 ± 1.72	6.81 ± 0.84	2.74 ± 0.15	<16.45	<207.44	AAA	< 9.31	9.34
J09494143+0037163	4	9.95 ± 1.00	6.73 ± 0.67	12.11 ± 1.25	24.63 ± 2.49						
	10	17.61 ± 1.79	10.99 ± 1.10	21.11 ± 2.82	35.16 ± 4.13						
	Total	13.29 ± 1.34	8.74 ± 0.88	17.63 ± 1.98	31.51 ± 3.33	87.09 ± 4.50	1254.62 ± 135.96	1364.04 ± 154.12	AAA	9.27	9.23
J09495263+0037043	4	10.84 ± 1.09	7.67 ± 0.77	14.83 ± 1.51	33.65 ± 3.38						
	10	23.41 ± 2.36	17.94 ± 1.80	31.27 ± 3.64	71.17 ± 7.44						
	Total	27.34 ± 2.99	20.07 ± 2.07	35.00 ± 7.65	81.32 ± 11.33	192.14 ± 9.94	3028.93 ± 328.16	4019.44 ± 421.57	AAA	9.68	9.62
J10205188+4831096	4	0.68 ± 0.07	0.52 ± 0.05	0.61 ± 0.06	2.82 ± 0.28						
	10	1.50 ± 0.15	1.12 ± 0.11	1.46 ± 0.15	5.80 ± 0.58						
	Total	2.15 ± 0.22	1.58 ± 0.16	1.73 ± 0.27	7.20 ± 0.73	14.76 ± 2.07	182.84 ± 19.85	276.01 ± 34.89	PAA	10.39	10.42
J10205369+4831246	4	1.40 ± 0.14	1.00 ± 0.10	0.63 ± 0.06	0.45 ± 0.04						
	10	2.85 ± 0.29	2.03 ± 0.20	1.36 ± 0.14	1.14 ± 0.12						
	Total	4.25 ± 0.43	2.91 ± 0.29	1.92 ± 0.27	2.04 ± 0.23	1.90 ± 0.27	<7.56	<72.13	PAA	< 9.78	9.72
J10272950+0114490	4	5.81 ± 0.58	4.38 ± 0.44	12.01 ± 1.20	36.28 ± 3.63						
	10	8.27 ± 0.83	5.91 ± 0.59	14.29 ± 1.45	42.18 ± 4.22						
	Total	8.27 ± 0.83	5.91 ± 0.59	14.29 ± 1.45	42.18 ± 4.22	53.17 ± 2.75	692.21 ± 75.02	1598.47 ± 173.13	AAA	10.28	10.32
J10272970+0115170	4	6.80 ± 0.68	4.49 ± 0.45	2.90 ± 0.29	1.96 ± 0.20						
	10	11.84 ± 1.18	7.81 ± 0.78	5.28 ± 0.59	3.93 ± 0.40						
	Total	16.04 ± 1.61	10.77 ± 1.08	8.09 ± 1.36	6.54 ± 0.69	1.75 ± 0.25	<22.95	<62.12	WAA	< 9.10	9.22
J10435053+0645466	4	3.48 ± 0.35	2.72 ± 0.27	7.53 ± 0.75	23.48 ± 2.35						
	10	7.29 ± 0.73	5.50 ± 0.55	15.40 ± 1.56	50.30 ± 5.03						
	Total	8.75 ± 0.88	6.55 ± 0.66	17.58 ± 1.91	57.33 ± 5.74	164.80 ± 8.52	1005.01 ± 108.90	1661.42 ± 175.97	APP	10.62	10.79
J10435268+0645256	4	2.01 ± 0.20	1.39 ± 0.14	1.62 ± 0.17	3.59 ± 0.36						
	10	3.86 ± 0.39	2.67 ± 0.27	3.33 ± 0.42	7.83 ± 0.78						
	Total	5.55 ± 0.56	3.83 ± 0.39	4.30 ± 1.20	9.93 ± 1.02	10.10 ± 0.52	94.53 ± 10.40	460.59 ± 67.12	APP	9.81	9.83
J10514368+5101195	4	10.13 ± 1.01	6.38 ± 0.64	4.30 ± 0.43	3.25 ± 0.33						
	10	18.89 ± 1.89	12.01 ± 1.20	7.87 ± 0.83	5.94 ± 0.60						
	Total	18.89 ± 1.89	12.01 ± 1.20	7.87 ± 0.83	5.94 ± 0.60	3.28 ± 0.14	55.62 ± 6.17	307.21 ± 56.37	AWW	9.51	9.40
J10514450+5101303	4	4.15 ± 0.41	2.66 ± 0.27	1.75 ± 0.18	1.14 ± 0.11						
	10	10.84 ± 1.08	7.02 ± 0.70	4.90 ± 0.56	3.41 ± 0.35						
	Total	10.84 ± 1.08	7.02 ± 0.70	4.90 ± 0.56	3.41 ± 0.35	<2.49	<17.44	<105.45	AAA	< 9.39	< 9.05
J12020424+5342317	4	0.64 ± 0.06	0.45 ± 0.04	0.26 ± 0.03	0.42 ± 0.04						
	10	1.70 ± 0.17	1.21 ± 0.12	0.88 ± 0.09	1.91 ± 0.19						
	Total	2.51 ± 0.25	1.78 ± 0.18	1.30 ± 0.19	3.12 ± 0.31	4.96 ± 0.29	48.56 ± 5.45	364.87 ± 52.62	AAA	10.44	10.18
J12020537+5342487	4	0.87 ± 0.09	0.69 ± 0.07	0.31 ± 0.03	0.26 ± 0.03						
	10	2.43 ± 0.24	1.70 ± 0.17	1.00 ± 0.10	0.66 ± 0.07						
	Total	3.91 ± 0.39	2.84 ± 0.28	1.73 ± 0.27	1.27 ± 0.13	<0.27	<6.88	<32.91	AAA	< 10.11	< 9.72

Table 3
(Continued)

(1) Galaxy ID	(2) Aperture (kpc)	(3) $f_{3.6\,\mu m}$ (mJy)	(4) $f_{4.5\,\mu m}$ (mJy)	(5) $f_{5.8\,\mu m}$ (mJy)	(6) $f_{8\,\mu m}$ (mJy)	(7) $f_{24\,\mu m}$ (mJy)	(8) $f_{70\,\mu m}$ (mJy)	(9) $f_{160\,\mu m}$ (mJy)	(10) Photometry	(11) TIR ($L_\odot$)	(12) L_{IR} ($L_\odot$)
J13082737+0422125	4	1.16 ± 0.12	0.78 ± 0.08	1.16 ± 0.12	2.87 ± 0.29						
	10	2.07 ± 0.21	1.36 ± 0.14	2.07 ± 0.27	5.31 ± 0.53						
	Total	2.35 ± 0.24	1.48 ± 0.16	1.99 ± 0.67	5.71 ± 0.61	5.91 ± 0.31	87.80 ± 9.67	336.59 ± 49.16	AAP	9.58	9.48
J13082964+0422045	4	2.49 ± 0.25	1.59 ± 0.16	1.60 ± 0.16	2.85 ± 0.28						
	10	4.04 ± 0.40	2.58 ± 0.26	2.92 ± 0.34	5.96 ± 0.60						
	Total	4.68 ± 0.47	2.98 ± 0.30	3.38 ± 0.64	7.43 ± 0.77	5.38 ± 0.28	87.55 ± 9.64	376.16 ± 63.60	AAP	9.61	9.53
J13325525−0301347	4	1.38 ± 0.14	1.04 ± 0.10	1.57 ± 0.16	5.60 ± 0.56						
	10	2.60 ± 0.26	1.91 ± 0.19	2.89 ± 0.29	10.49 ± 1.05						
	Total	3.25 ± 0.33	2.34 ± 0.23	3.30 ± 0.35	11.50 ± 1.15	46.50 ± 6.51	497.48 ± 53.92	575.53 ± 67.59	PPP	10.68	10.64
J13325655−0301395	4	0.88 ± 0.09	0.60 ± 0.06	0.46 ± 0.05	1.23 ± 0.12						
	10	2.82 ± 0.28	1.89 ± 0.19	2.23 ± 0.22	7.44 ± 0.74						
	Total	5.29 ± 0.53	3.62 ± 0.36	4.50 ± 0.48	15.98 ± 1.60	15.94 ± 2.23	176.01 ± 19.19	770.98 ± 85.21	PPP	10.53	10.52
J13462001−0325407	4	5.26 ± 0.53	3.65 ± 0.36	2.93 ± 0.30	3.11 ± 0.31						
	10	9.04 ± 0.90	6.08 ± 0.61	5.38 ± 0.59	6.97 ± 0.70						
	Total	11.83 ± 1.19	7.84 ± 0.79	7.64 ± 1.59	11.03 ± 1.12	13.99 ± 0.72	51.49 ± 5.85	692.82 ± 74.59	AAA	9.80	9.79
J13462215−0325057	4	5.42 ± 0.54	3.60 ± 0.36	2.59 ± 0.26	2.25 ± 0.22						
	10	7.36 ± 0.74	4.86 ± 0.49	3.31 ± 0.40	2.75 ± 0.28						
	Total	9.06 ± 0.91	5.96 ± 0.60	3.23 ± 1.09	3.28 ± 0.36	6.15 ± 0.32	41.13 ± 4.83	<77.92	AAA	< 9.13	9.34
J14005782+4251207	4	3.80 ± 0.38	3.41 ± 0.34	8.21 ± 0.82	26.57 ± 2.66						
	10	6.88 ± 0.69	5.37 ± 0.54	11.80 ± 1.19	40.61 ± 4.06						
	Total	10.07 ± 1.02	7.17 ± 0.72	14.42 ± 2.01	49.30 ± 4.93	94.87 ± 13.28	1218.70 ± 132.05	1697.41 ± 184.78	PPP	10.76	10.81
J14005882+4250427	4	5.36 ± 0.54	4.22 ± 0.42	12.09 ± 1.21	39.95 ± 3.99						
	10	7.41 ± 0.74	5.80 ± 0.58	15.95 ± 1.60	54.19 ± 5.42						
	Total	8.86 ± 0.89	6.35 ± 0.64	16.23 ± 1.91	55.36 ± 5.54	190.59 ± 26.68	1470.53 ± 159.33	1786.75 ± 204.99	PPP	10.87	10.97
J14250552+0313590	4	3.63 ± 0.36	2.69 ± 0.27	2.16 ± 0.22	2.38 ± 0.24						
	10	5.68 ± 0.57	3.99 ± 0.40	3.18 ± 0.33	3.48 ± 0.35						
	Total	6.72 ± 0.67	4.67 ± 0.47	3.55 ± 0.43	3.74 ± 0.39	9.66 ± 0.50	111.32 ± 12.18	526.61 ± 60.98	AAA	10.11	9.83
J14250739+0313560	4	1.18 ± 0.12	0.77 ± 0.08	0.48 ± 0.05	0.31 ± 0.03						
	10	1.63 ± 0.16	1.05 ± 0.10	0.66 ± 0.10	0.52 ± 0.06						
	Total	1.63 ± 0.16	1.05 ± 0.10	0.66 ± 0.10	0.52 ± 0.06	1.39 ± 0.19	<9.15	<104.79	WAA	< 9.55	8.98
J14334683+4004512	4	6.67 ± 0.67	4.75 ± 0.48	8.79 ± 0.88	23.43 ± 2.34						
	10	11.98 ± 1.20	8.12 ± 0.81	12.27 ± 1.24	30.52 ± 3.05						
	Total	19.27 ± 1.93	12.93 ± 1.30	19.74 ± 2.32	47.21 ± 4.73	86.65 ± 4.48	840.66 ± 91.10	1747.03 ± 185.16	PPP	10.49	10.57
J14334840+4005392	4	10.27 ± 1.03	7.11 ± 0.71	19.60 ± 1.96	60.41 ± 6.04						
	10	14.36 ± 1.44	9.95 ± 0.99	27.36 ± 2.74	85.42 ± 8.54						
	Total	16.50 ± 1.65	11.43 ± 1.15	29.35 ± 3.06	91.71 ± 9.17	117.17 ± 6.06	1337.09 ± 144.88	2553.35 ± 269.55	PPP	10.66	10.79
J14530282+0317451	4	17.75 ± 1.78	13.12 ± 1.31	18.41 ± 1.94	42.39 ± 4.24						
	10	26.86 ± 2.69	26.41 ± 2.64	22.96 ± 4.43	57.36 ± 5.74						
	Total	26.86 ± 2.69	26.41 ± 2.64	22.96 ± 4.43	57.36 ± 5.74	47.05 ± 2.43	680.55 ± 73.76	3028.63 ± 320.69	AAA	9.18	9.11
J14530523+0319541	4	25.20 ± 2.52	16.15 ± 1.62	13.88 ± 1.52	23.56 ± 2.38						
	10	45.99 ± 4.61	31.66 ± 3.19	31.69 ± 4.94	90.85 ± 9.08						
	Total	49.18 ± 4.94	35.19 ± 3.59	33.88 ± 7.17	117.68 ± 11.77	50.07 ± 2.59	830.04 ± 89.96	2432.15 ± 259.60	AAA	9.14	9.29
J15064391+0346364	4	4.37 ± 0.44	2.73 ± 0.27	1.84 ± 0.18	1.30 ± 0.13						
	10	7.20 ± 0.72	4.59 ± 0.46	3.18 ± 0.33	2.37 ± 0.24						
	Total	9.04 ± 0.90	5.67 ± 0.57	3.81 ± 0.52	2.92 ± 0.32	2.22 ± 0.31	36.79 ± 4.35	<141.61	WAA	< 9.82	9.45
J15064579+0346214	4	4.45 ± 0.45	4.34 ± 0.43	6.10 ± 0.61	11.95 ± 1.19						
	10	7.22 ± 0.72	6.25 ± 0.62	8.89 ± 0.89	20.05 ± 2.00						
	Total	9.61 ± 0.96	7.72 ± 0.77	10.95 ± 1.19	26.50 ± 2.66	47.67 ± 2.47	340.83 ± 36.98	1440.24 ± 156.70	AAA	10.55	10.57
J15101587+5810425	4	3.47 ± 0.35	2.22 ± 0.22	1.51 ± 0.15	1.22 ± 0.12						
	10	5.54 ± 0.55	3.61 ± 0.36	2.69 ± 0.29	2.83 ± 0.28						
	Total	6.28 ± 0.63	4.07 ± 0.41	3.16 ± 0.35	4.13 ± 0.41	2.86 ± 0.40	31.00 ± 3.62	<62.28	PPA	< 9.37	9.50
J15101776+5810375	4	2.46 ± 0.25	1.78 ± 0.18	2.87 ± 0.29	8.28 ± 0.83						
	10	4.83 ± 0.48	3.41 ± 0.34	6.28 ± 0.64	18.22 ± 1.82						
	Total	5.01 ± 0.50	3.50 ± 0.35	6.45 ± 0.65	18.62 ± 1.86	27.91 ± 3.91	384.68 ± 41.70	1160.61 ± 124.37	PPA	10.39	10.30
J15281276+4255474	4	15.92 ± 1.59	10.57 ± 1.06	14.35 ± 1.44	33.82 ± 3.38						
	10	31.74 ± 3.17	20.64 ± 2.06	32.36 ± 3.26	74.22 ± 7.42						
	Total	33.68 ± 3.37	24.95 ± 2.50	37.27 ± 4.63	81.05 ± 8.16	93.80 ± 4.85	1524.48 ± 165.19	3472.94 ± 365.14	AAA	10.43	10.41
J15281667+4256384	4	14.02 ± 1.40	8.93 ± 0.89	6.26 ± 0.63	5.04 ± 0.50						
	10	18.60 ± 1.86	11.71 ± 1.17	7.95 ± 0.89	6.17 ± 0.63						
	Total	24.34 ± 2.44	13.20 ± 1.33	7.98 ± 1.89	7.21 ± 0.92	4.25 ± 0.22	123.94 ± 13.59	252.58 ± 32.84	AAA	9.29	9.23
J15562191+4757172	4	2.94 ± 0.29	2.11 ± 0.21	5.31 ± 0.53	15.16 ± 1.52						
	10	5.61 ± 0.56	3.84 ± 0.39	7.95 ± 0.85	21.14 ± 2.11						
	Total	6.48 ± 0.65	4.40 ± 0.45	8.85 ± 1.22	22.15 ± 2.22	48.79 ± 2.44	538.73 ± 58.40	1163.05 ± 125.91	AAA	10.06	10.03
J15562738+4757302	4	3.63 ± 0.36	2.26 ± 0.23	1.45 ± 0.15	0.90 ± 0.09						
	10	4.93 ± 0.49	3.06 ± 0.31	1.79 ± 0.36	1.24 ± 0.13						
	Total	5.07 ± 0.51	3.12 ± 0.32	1.76 ± 0.64	1.33 ± 0.16	<0.35	<7.34	<30.31	AAA	< 9.05	< 8.66
J16024254+4111499	4	2.89 ± 0.29	2.15 ± 0.22	6.78 ± 0.68	22.67 ± 2.27						
	10	7.02 ± 0.70	5.04 ± 0.50	20.88 ± 2.11	53.41 ± 5.34						
	Total	11.04 ± 1.11	7.88 ± 0.79	22.89 ± 2.43	77.56 ± 7.76	109.52 ± 15.33	1110.58 ± 120.33	2171.84 ± 237.03	PPP	10.82	10.96
J16024475+4111589	4	1.72 ± 0.17	1.17 ± 0.12	3.29 ± 0.33	9.50 ± 0.95						
	10	3.64 ± 0.36	2.58 ± 0.26	6.74 ± 0.69	21.92 ± 2.19						
	Total	3.64 ± 0.36	2.58 ± 0.26	6.74 ± 0.69	21.92 ± 2.19	26.83 ± 3.76	460.22 ± 49.90	1143.07 ± 146.32	PPP	10.46	10.39

Table 3
(Continued)

(1) Galaxy ID	(2) Aperture (kpc)	(3) $f_{3.6\,\mu m}$ (mJy)	(4) $f_{4.5\,\mu m}$ (mJy)	(5) $f_{5.8\,\mu m}$ (mJy)	(6) $f_{8\,\mu m}$ (mJy)	(7) $f_{24\,\mu m}$ (mJy)	(8) $f_{70\,\mu m}$ (mJy)	(9) $f_{160\,\mu m}$ (mJy)	(10) Photometry	(11) L_{TIR} ($L_\odot$)	(12) L_{IR} ($L_\odot$)
J17045089+3448530	4	1.11 ± 0.11	0.84 ± 0.08	1.06 ± 0.11	4.62 ± 0.46						
	10	2.47 ± 0.25	1.80 ± 0.18	2.63 ± 0.27	13.13 ± 1.31						
	Total	2.82 ± 0.28	2.07 ± 0.21	2.94 ± 0.31	15.88 ± 1.59	28.93 ± 4.05	82.28 ± 9.07	360.76 ± 48.50	PPP	10.49	10.80
J17045097+3449020	4	2.56 ± 0.26	2.25 ± 0.23	4.56 ± 0.46	23.63 ± 2.36						
	10	5.07 ± 0.51	3.99 ± 0.40	8.83 ± 0.88	49.86 ± 4.99						
	Total	5.56 ± 0.56	4.25 ± 0.43	8.71 ± 0.88	47.99 ± 4.80	131.22 ± 18.37	1518.03 ± 164.47	1636.24 ± 175.34	PPP	11.31	11.36
J20471908+0019150	4	33.53 ± 3.35	18.87 ± 1.89	14.31 ± 1.44	10.86 ± 1.09						
	10	61.20 ± 6.12	34.60 ± 3.46	27.27 ± 2.82	25.13 ± 2.55						
	Total	132.43 ± 13.43	75.75 ± 7.63	66.41 ± 16.73	101.26 ± 13.41	121.03 ± 6.27	462.86 ± 50.18	3048.90 ± 326.39	AAA	10.02	10.24
J20472428+0018030	4	21.05 ± 2.10	13.11 ± 1.31	8.92 ± 0.90	5.76 ± 0.58						
	10	36.97 ± 3.70	23.40 ± 2.34	15.72 ± 1.74	10.50 ± 1.13						
	Total	50.90 ± 5.12	31.05 ± 3.11	22.91 ± 4.75	16.23 ± 2.88	11.93 ± 0.62	<36.64	<117.51	AAA	< 9.10	9.32
J13153076+6207447	4	6.00 ± 0.60	4.00 ± 0.40	15.00 ± 1.50	46.00 ± 4.60						
	10	8.00 ± 0.80	6.00 ± 0.60	18.00 ± 1.80	54.00 ± 5.40						
	Total	8.00 ± 0.80	6.00 ± 0.60	18.00 ± 1.80	54.00 ± 5.40					11.01	11.01
J13153506+6207287	4	16.00 ± 1.60	15.00 ± 1.50	59.00 ± 5.90	179.00 ± 17.90						
	10	17.00 ± 1.70	16.00 ± 1.60	62.00 ± 6.20	187.00 ± 18.70						
	Total	17.00 ± 1.70	16.00 ± 1.60	62.00 ± 6.20	187.00 ± 18.70					11.65	11.65

Notes. Descriptions of columns: 1. Galaxy ID; 2. Diameter of IRAC aperture; 3. Flux density in the IRAC 3.6 μm band; 4. Flux density in the IRAC 4.5 μm band; 5. Flux density in the IRAC 5.8 μm band; 6. Flux density in the IRAC 8.0 μm band; 7. Flux density in the MIPS 24 μm band; 8. Flux density in the MIPS 70 μm band; 9. Flux density in the MIPS 160 μm band; 10. Photometry methods for measurements of MIPS flux densities. "A" stands for aperture photometry, "W" for weak source, and "P" for PRF fitting. The three letters correspond to the 24, 70, and 160 μm bands, respectively. For example, "AAP" means that flux densities in both the 24 and 70 μm bands were measured by aperture photometry while the 160 μm flux density was measured by PRF fitting; 11. Logarithm of the L_{TIR}, calculated from $L_{24\,\mu m}$, $L_{70\,\mu m}$, and $L_{160\,\mu m}$ using the formula of Dale & Helou (2002); 12. Logarithm of the L_{IR}, an unbiased estimator of the L_{TIR} calculated from $L_{24\,\mu m}$ and $L_{8\,\mu m}$.

4. IR EMISSION OF PAIRED GALAXIES—IMAGES AND CATALOGS

Spitzer images at 3.6, 8.0, 24, and 70 μm are presented in Figure 1 for all pairs in our sample except for KPAIR J1315+6207 (UGC08335a/b). These are grayscale images overlaid by contours. The contour levels are $S_{bg} + S_0 \times 2^n$ ($n = 0$, 1, 2,...), where S_{bg} is the local background level and $S_0 = 0.032$, 0.16, 0.28, and 2.0 MJy sr^{-1} for the 3.6, 8.0, 24, and 70 μm bands, respectively. The S_0 values are the sample medians of the 4σ threshold of the corresponding bands. The sizes of all images are $2' \times 2'$ except for the three large pairs: J0949+0037, J1453+0317, and J2047+0019, for which a scale bar of length of $2'$ is given. We chose not to present the images in the other three *Spitzer* bands because: (1) the images of the 4.5 μm emission have nearly identical morphology as their 3.6 μm counterparts, (2) the 5.8 μm array is the most noisy among the IRAC detector arrays, and (3) the angular resolution of the 160 μm band, FWHM = 40″, is so coarse that little information can be gained from the images in addition to what is already given by the f_{160} of component galaxies listed in Table 3.

The flux densities of KPAIR galaxies, in all seven *Spitzer* bands, are listed in Table 3. For the four IRAC bands, aperture photometry corresponding to physical diameters of 4 and 10 kpc are also provided. The methods and error estimates are discussed previously in Section 3. For non-detections, 4σ upper limits are given. All galaxies in our sample are detected in IRAC bands. The detection rates are 47/52, 40/52, and 36/52 for the MIPS 24 μm, 70 μm, and 160 μm bands, respectively.

Listed are also two estimates of the total IR (3–1000 μm) luminosities. The L_{TIR} is derived using the formula of Dale et al. (2005):

$$L_{TIR} = 1.559 \times L_{24} + 0.7686 \times L_{70} + 1.374 \times L_{160}, \quad (1)$$

where L_{24}, L_{70}, and L_{160} are the monochromatic luminosities (νL_ν). Another IR luminosity is defined using the 24 and 8 μm flux densities:

$$\log(L_{IR}) = \log(L_{24}) + 0.87(\pm 0.03) + 0.56(\pm 0.09) \times \log(L_8/L_{24}), \quad (2)$$

where L_{24} and L_8 are again the monochromatic luminosities (νL_ν). L_{IR} is an unbiased approximation of L_{TIR}. It was derived from the linear regression of the $\log(L_{24}/L_{TIR})$ versus $\log(L_8/L_{24})$ correlation using data of 34 spiral galaxies in the KPAIR sample that are detected in all *Spitzer* bands (the left panel of Figure 2), exploiting a similar method that was originally developed by Calzetti et al. (2005). The result is nearly identical for a linear regression with the galaxies containing active galactic nuclei (AGNs; three of them) excluded. A comparison between $\log(L_{TIR})$ and $\log(L_{IR})$ is plotted in the right panel of Figure 2. Indeed there is a very tight linear correlation between them, with a dispersion of only 0.11. Given the better detection rate of L_{IR} than that of L_{TIR} and the tight linear correlation between the two, we will use L_{IR} hereafter whenever total IR luminosities are invoked in calculations.

The images and photometry show very diversified IR emission properties among KPAIR galaxies. We verify that, except for those with AGNs, paired E galaxies have very low dust emission ($\log(L_{IR}/L_\odot) \sim 9$–10), indicating little star formation occurring in them. Among the paired spiral galaxies, the majority have rather moderate IR luminosity ($\sim 10^{10}\,L_\odot$). There are six known AGNs (Table 1), three in S galaxies and three in E galaxies. There are four LIRGs (one of them being an AGN), but no ULIRGs, in the sample. Some detailed notes on individual pairs can be found in Appendix A.

5. STAR FORMATION ENHANCEMENT

5.1. Control Sample of Single Late-type Galaxies

In this section, SFRs of 39 non-AGN spiral galaxies in the KPAIR sample are compared with those of single galaxies in a control sample. In order to have a clean comparison, we chose to select a control sample that also contains 39 spiral galaxies,

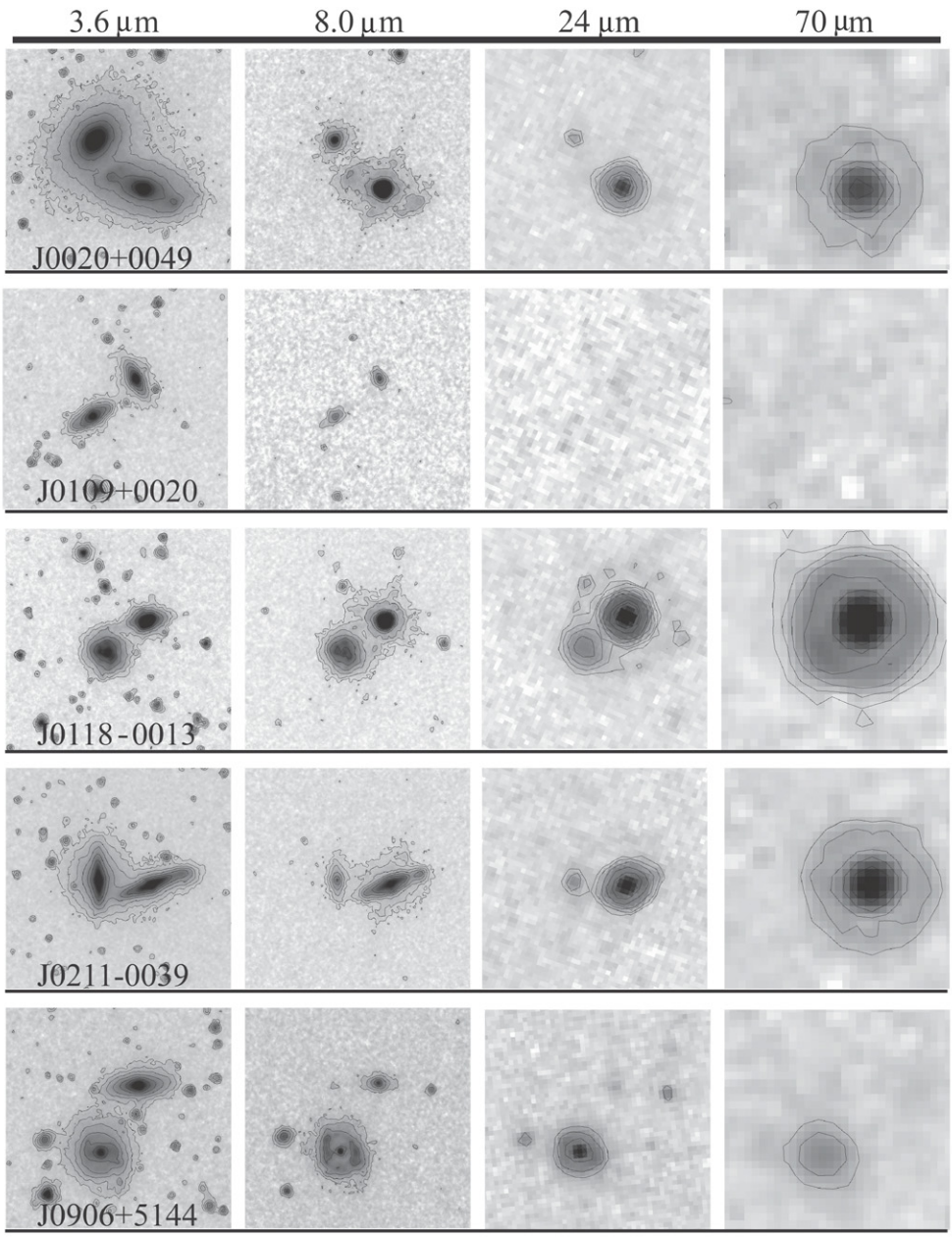

Figure 1. *Spitzer* images of galaxy pairs. The contour levels are $S_{\rm bg} + S_0 \times 2^n$ ($n = 0, 1, 2,...$), where $S_{\rm bg}$ is the local background level and S_0, the sample median of the 4σ threshold of the corresponding bands, are 0.032, 0.16, 0.28, and 2.0 MJy sr^{-1} for the 3.6 μm, 8.0 μm, 24 μm, and 70 μm bands, respectively. The sizes of all images are $2' \times 2'$ except for the three large pairs: J0949+0037, J1453+0317, and J2047+0019, for which a scale bar of length of $2'$ is given.

each matching a spiral galaxy in the pair sample of the same mass.

The selection of the control sample was confined to two *Spitzer* data archives. (1) The SWIRE survey of Lockman field and ELAIS-N1 field (covering ~ 20 deg^2; Lonsdale et al. 2003), which provides an IRAC 3.6 μm band selected sample of field galaxies (Surace et al. 2005). The restriction to the Lockman and ELAIS-N1 fields is because these regions in the SWIRE survey have good SDSS spectroscopic coverages (Abazajian et al. 2005). (2) The SINGS survey of nearby galaxies (Kennicutt et al. 2003), which observed a heterogeneously selected sample of 75 well-known galaxies, including normal late and early types, AGNs, and starbursts.

The criteria for a galaxy to be considered in the selection of the control sample are:

1. has published *Spitzer* IRAC and MIPS data;
2. has spectroscopic redshift, and $z \leqslant 0.1$;
3. K_s, taken from the K_{20} of 2MASS, $\leqslant 13.5$ mag;
4. is a late-type galaxy outside any interacting system; and
5. does not have a known AGN.

Paired spiral galaxies with $\log(M/M_\odot) \geqslant 10.3$ were matched with single galaxies in the two SWIRE fields. Their *Spitzer* flux densities were taken from the SWIRE Data Release 2 (Surace et al. 2005). For both IRAC 8 μm and MIPS 24 μm bands, the Kron fluxes (and the associated errors) are adopted. For f_{24}, an additional 15% aperture correction is applied (Shupe et al. 2008). SDSS images were inspected and galaxies showing signs of interaction or being in pairs were excluded. These single galaxies were separated into two morphological types, "S" or "E," using the same scheme as for the classification of

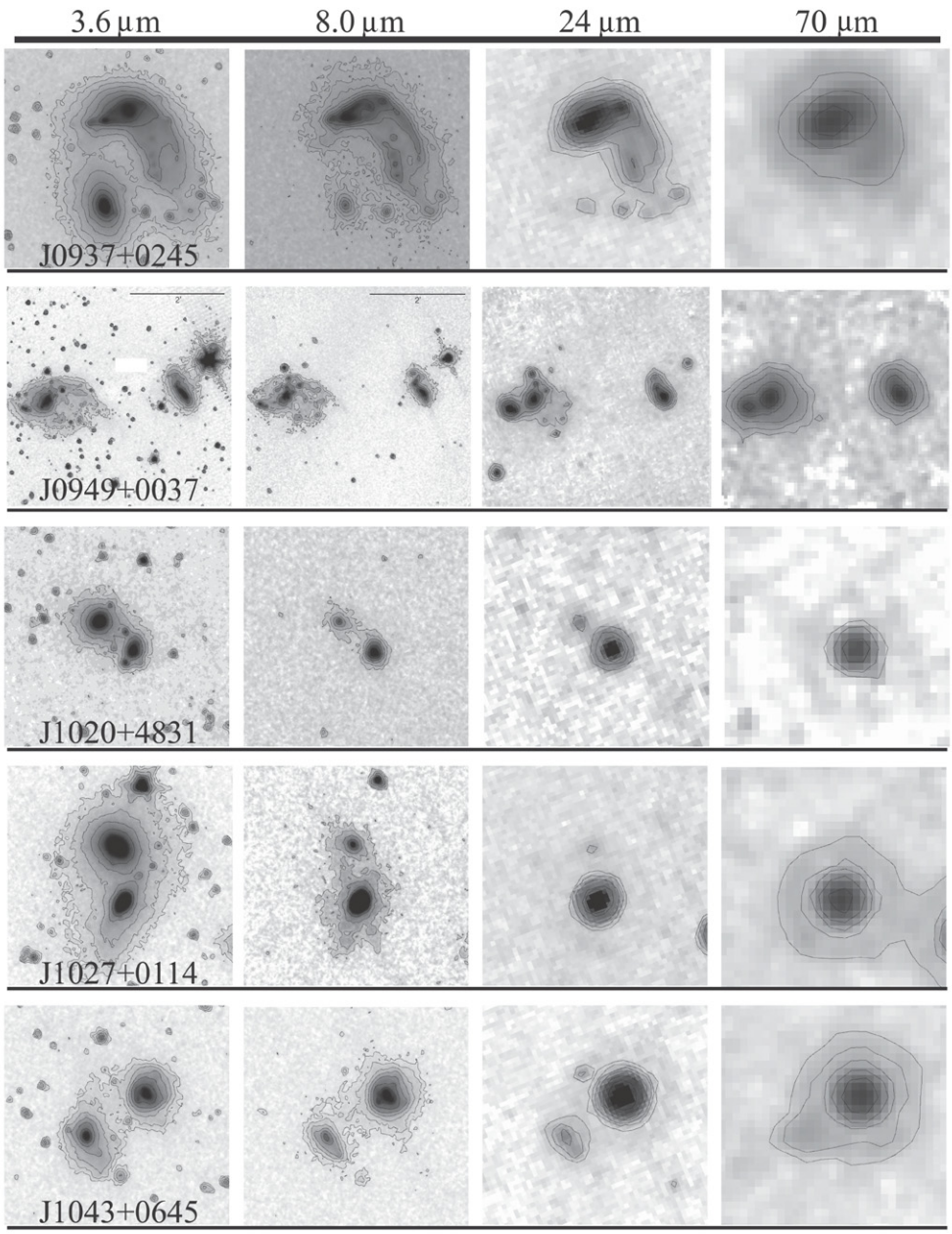

Figure 1. (Continued)

paired galaxies (see Section 2). Then, each non-AGN spiral galaxy in the KPAIR sample is matched by one of the 88 single spiral galaxies so selected, according to the following requirements: (1) the single galaxy should have $\log(M)$ within ± 0.1 of that of the paired galaxy; and (2) among all single spiral galaxies fulfilling requirement (1), the chosen one should have the minimum redshift difference from that of the paired galaxy. It should be pointed out that, despite requirement (2), there is still a significant difference between redshift distributions of the paired galaxies and of single galaxies in the control sample: the medians are $z = 0.031$ and $z = 0.046$, respectively. This is because of the pair selection criterion 1 (see Section 2) that requires the primaries are brighter $K_s = 12.5$ mag, while the control sample is selected from galaxies brighter than $K_s = 13.5$ mag. We argue that the redshift difference will not introduce any bias (in particular the Malmquist bias) into the comparisons between the two samples that are mass-matched, because all mass-normalized properties (e.g., the light-to-mass ratio, SFR/M, etc.) shall not depend on redshift in these local samples,[9] for which the cosmic evolutionary effects are negligible. Indeed, requirement (2) is arguably disposable, and any galaxy fulfilling requirement (1) could have been included in the control sample. In order to assess the uncertainties due to the particular choice of the selected control sample, a Monte Carlo analysis (100 repeats) was carried out. In each of the 100 realizations, an alternative control sample was selected by relaxing requirement (2) and choosing arbitrarily the match of any KPAIR galaxy among galaxies fulfilling requirement (1). Then the same statistics of the star formation properties that were calculated using the official control sample (see the following

[9] This insensitivity of mass-normalized properties to any selection effect is the major reason for us to choose the one-to-one mass-matching method of control sample selection.

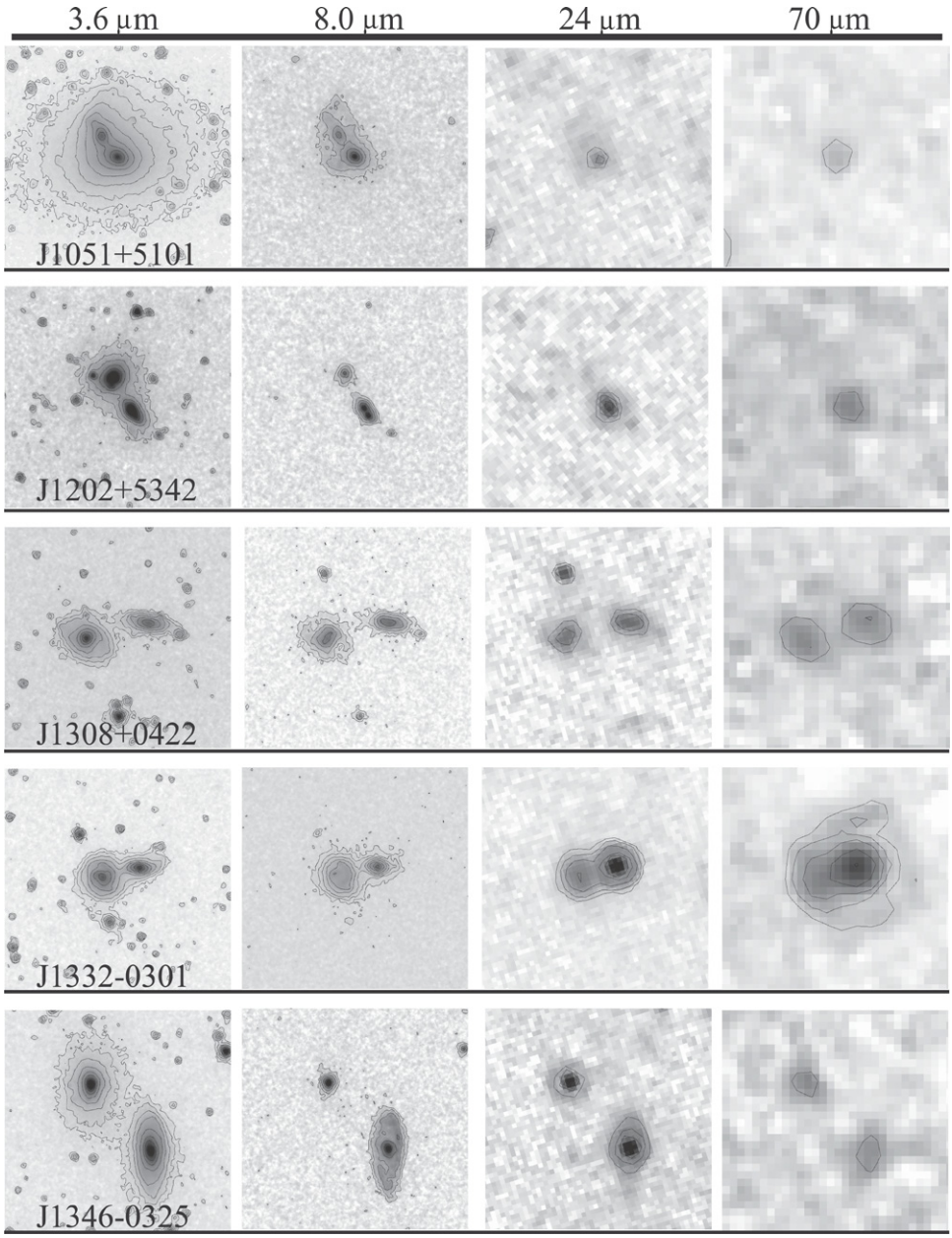

Figure 1. (Continued)

sections) were repeated using the alternative control sample. We confirm that for any of these statistics, the mean of the 100 realizations is consistent with the result derived from the official control sample within 1σ.

There are no single spiral galaxies among the selected SWIRE sources that have $\log(M/M_{\odot}) < 10.3$, while five KPAIR-S galaxies have mass less than this limit. These paired spirals were matched by non-interacting normal spiral galaxies in the SINGS sample. There are only six such SINGS galaxies in this mass range. The same requirements that were applied to the SWIRE galaxies were applied here, except for NGC 3418 whose mass differs from that of its match (J14530523+0319541) by 0.14 dex (the closest match), slightly exceeding the limit of 0.10 dex. The 8 and 24 μm data of SINGS galaxies were taken from Smith et al. (2007). All galaxies in the control sample, together with their matches in the KPAIR sample, are listed in Table 4.

5.2. Star Formation Enhancement in Paired Non-AGN Spirals

The SFR of a galaxy can be estimated from the IR luminosity using the formula of Kennicutt (1998):

$$\mathrm{SFR}\,(M_{\odot}\ \mathrm{yr}^{-1}) = 4.510 \times 10^{-44} \times L_{\mathrm{IR}}\ (\mathrm{erg\ s}^{-1}). \quad (3)$$

Note that this estimate is contaminated by the dust emission powered by the radiation of old stars. Also, it does not include the UV radiation of young stars that is not absorbed by dust. For an average normal spiral galaxy, both biases are at the $\sim 30\%$ level (Buat & Xu 1996). Under the assumption that they affect the KPAIR sample and the control sample in the same way, this estimator is exploited in the comparison between the SFR of the two samples. However, when comparing our results with other works using different star formation indicators (e.g., the UV continuum and the optical emission lines), the biases should be taken into account (Iglesias-Paramo et al. 2004).

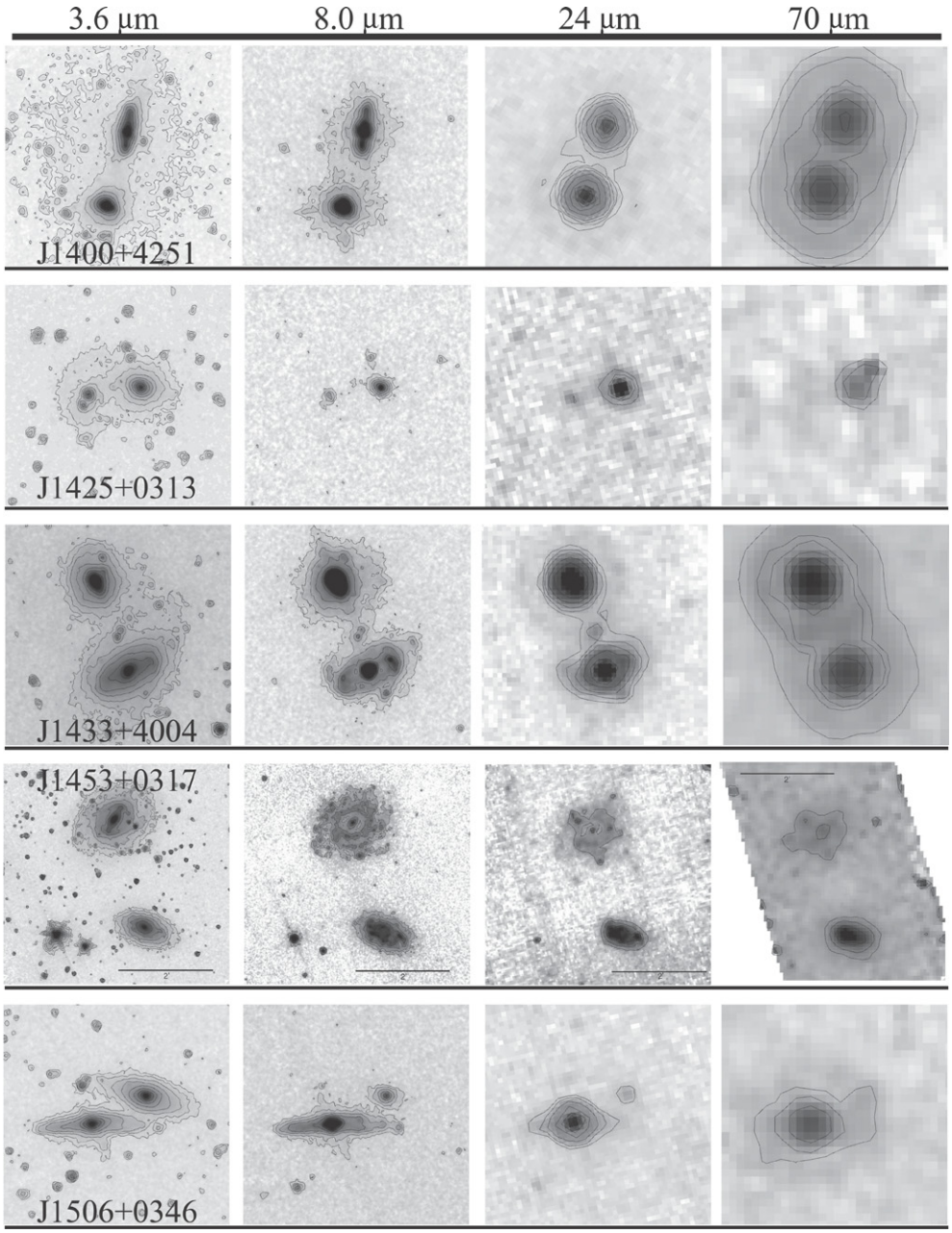

Figure 1. (Continued)

There are two L_{IR} upper limits in the sample of KPAIR spirals, and two in the control sample. In what follows, in any of the statistical analyses involving L_{IR}, all upper limits were replaced by numbers of half of the values and treated as detections. We confirm that there is no significant difference whether these upper limits are or are not included in the analyses.

In Figure 3, a histogram of $\log(L_{IR})$ ($\log(SFR)$) of non-AGN spirals in the KPAIR sample (KPAIR-S) is compared to that of the single spirals in the control sample (CONTROL). There is a striking difference between the two distributions: while the distribution of CONTROL has a single prominent peak at $\log(L_{IR}) = 9.75$ (SFR $\sim 1\,M_{\odot}$ yr^{-1}), the distribution of KPAIR-S has a second peak at much enhanced L_{IR} level of $\log(L_{IR}) = 10.65$, corresponding to SFR $\sim 8\,M_{\odot}$ yr^{-1}. There is a significant excess of KPAIR-S galaxies in the high L_{IR} end. Indeed, while three non-AGN spiral galaxies in the KPAIR sample are in the LIRG category ($\log(L_{IR}) > 11$), none of the galaxies in the control sample is a LIRG. The Kolmogorov–Smirnov test (K–S test) of the SFR distributions yields a rather low probability of 3.9%, or equivalently a rejection at 96.1% confidence level, for the null hypotheses that the two samples are drawn from the same population. The mean $\log(L_{IR})$ for the KPAIR-S sample is $\log(L_{IR}) = 10.13 \pm 0.12$, corresponding to a mean $\log(SFR) = 0.36 \pm 0.12$. For the CONTROL sample, the means are $\log(L_{IR}) = 9.84 \pm 0.08$ and $\log(SFR) = 0.07 \pm 0.08$. The Student's t-test yields a score of 2.32, corresponding to a probability of 2.6% for the null hypotheses that the means of the two samples are equal, consistent with the result of the K–S test.

Figure 4 is a comparison of histograms of sSFR, i.e., SFR per mass (SFR/M), of the same two samples. It shows a similar shift of the distribution of KPAIR-S galaxies toward the higher

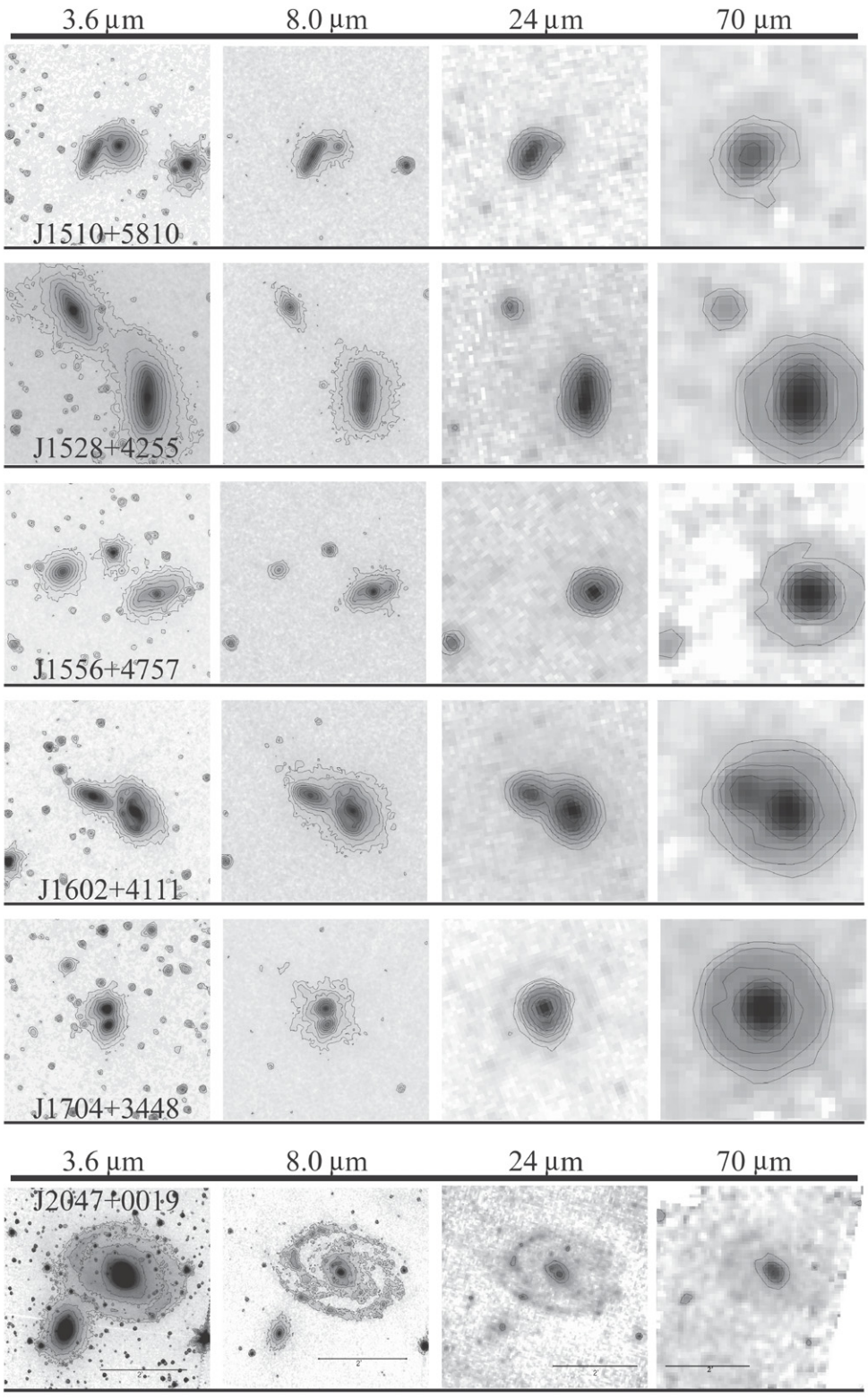

Figure 1. (Continued)

SFR/M bins compared to the control sample, although the difference is slightly less prominent than that shown in Figure 3. Indeed, eight KPAIR-S galaxies have SFR/$M > 10^{-10}$ yr^{-1} while only one galaxy in the control sample has such high SFR/M. The K–S test of the SFR/M distribution finds a low probability for the null hypotheses of 3.9%. The mean values of log(SFR/M) are -10.50 ± 0.10 and -10.78 ± 0.08 for the non-AGN spirals in the KPAIR sample and in the control sample, respectively. The score of the Student's t-test of the means is 2.21, and the probability for the null hypotheses is only 3.3%.

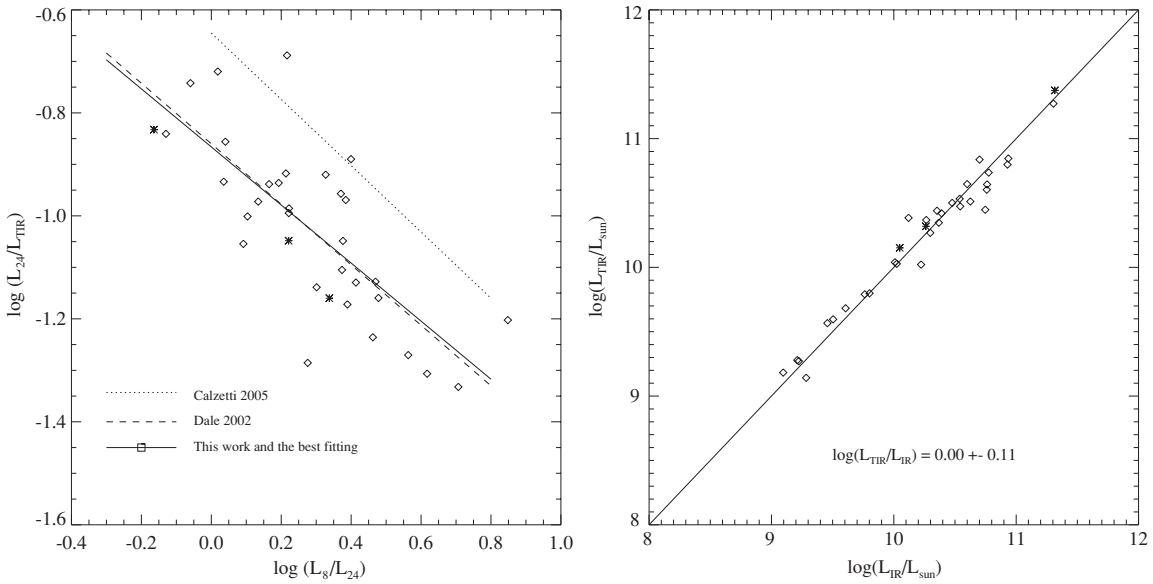

Figure 2. Left: $\log(L_{24}/L_{\rm TIR})$ vs. $\log(L_8/L_{24})$ plot of spiral galaxies (diamonds: without AGNs; eight-point stars: with AGNs) in the KPAIR sample, detected in all *Spitzer* bands. The solid line is a linear regression of the data. The dotted line is the relation found by Calzetti et al. (2005) for star formation regions in M51. The dashed line, also taken from Calzetti et al. (2005), is the prediction of the model of Dale & Helou (2002) for galaxies. Right: $\log(L_{\rm TIR})$ vs. $\log(L_{\rm IR})$ plot of same galaxies, where $\log(L_{\rm IR}) = \log(L_{24}) + 0.87 + 0.56 \times \log(L_8/L_{24})$.

5.3. Mass Dependence of SFR/M Enhancement in Paired Spirals

In order to study mass dependence of the SFR and its enhancement in galaxy pairs, we binned the spirals both in the KPAIR sample and in the control sample into four mass bins, and calculated the means of $\log(\mathrm{SFR}/M)$ for individual bins. The results are listed in Table 5 and plotted in Figure 5. Galaxies in the control sample show a clear trend of decreasing sSFR with increasing mass, as has already been well documented in the literature (Kauffmann et al. 2004; Brinchmann et al. 2004; Schiminovich et al. 2007; Zheng et al. 2007). On the other hand, the sSFR of spirals in pairs is nearly constant with mass. In the lowest mass bin of $9.7 < \log(M/M_\odot) < 10.2$, there is no enhancement of the sSFR of the paired galaxies compared to that of the control sample. And at the high-mass end, in the bin of $11.3 < \log(M/M_\odot) < 11.6$, the mean sSFR of the paired galaxies is about three times higher than that of the control sample. In between, there is a weak enhancement in the two intermediate mass bins.

5.4. Comparison of Non-AGN Spirals in S+S and in S+E Pairs

Sulentic (1989) and Xu & Sulentic (1991) found significant FIR enhancement in S+E pairs in their *IRAS* studies, under the assumption that the ellipticals in these pairs are FIR quiet. However, the *ISO* observations of Domingue et al. (2003) demonstrated that this assumption is invalid. In this section, we address again the question whether spiral galaxies in S+E pairs have similar levels of SFR enhancement as those in S+S pairs.

In Figure 6, the non-AGN spirals in the KPAIR sample are decomposed into two subsamples, one for galaxies in S+S pairs (28 galaxies) and the other for galaxies in S+E pairs (11 galaxies), and the $\log(\mathrm{SFR}/M)$ distribution of each of them is compared to that of the control sample in one of the two panels. Because here the samples being compared do not have the same numbers of sources, the distributions are normalized (i.e., in fractions). It shows that the distribution of the S galaxies in S+E pairs is *not* significantly different from that of the control

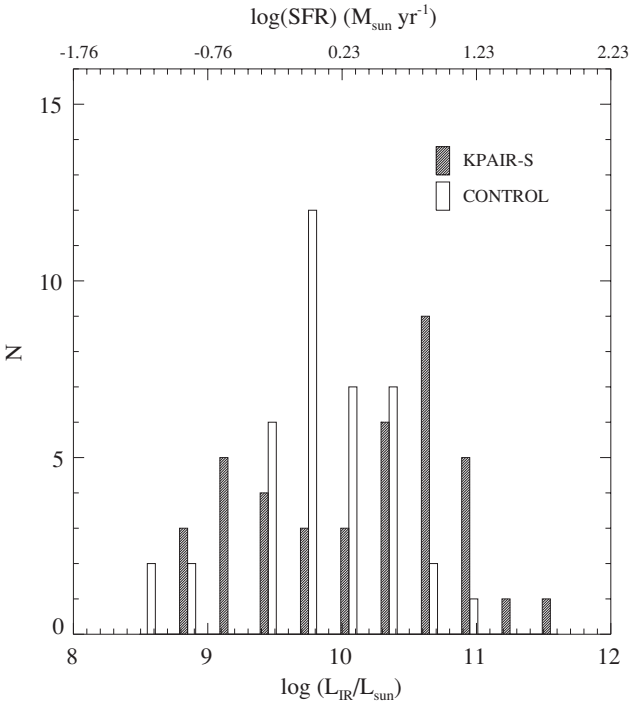

Figure 3. Histograms of $\log(L_{\rm IR})$ distributions of the non-AGN spirals in the KPAIR sample ("KPAIR-S") and of the control sample. Corresponding log(SFR) values are marked on the top.

sample: the K–S test finds a 91% probability that the two samples are drawn from the same population. Therefore, all the enhancement found in Figure 4 is due to spirals in the S+S pairs. For the comparison between the spirals in S+S sample and the control sample, the K–S test yields a probability of only 2% for the null hypotheses. The average values of $\log(\mathrm{SFR}/M)$ are -10.36 ± 0.11 and -10.88 ± 0.19 for spirals in S+S sample and in S+E sample, respectively.

In Figure 7, the mass dependence of SFR/M is plotted for non-AGN spirals in S+S pairs and in S+E pairs, separately. No significant enhancement is found for spirals in S+E pairs in any

Table 4
Galaxies in the Control Sample and Their KPAIR Matches (Non-AGN Spirals)

(1) Galaxy ID	(2) Coordinates (J2000)	(3) z	(4) K_s (mag)	(5) $f_{8\,\mu m}$ (mJy)	(6) $f_{24\,\mu m}$ (mJy)	(7) log(M) ($M_\odot$)	(8) log(sSFR) (yr^{-1})	(9) KPAIR Galaxy ID	(10) z	(11) log(M) ($M_\odot$)	(12) log(sSFR) (yr^{-1})	(13) ϵ	(14) CAT	(15) SEP
LCK-287434	10h58m58.^{s}0+58d08m01s	0.0320	12.17	7.94 ± 0.02	6.76 ± 0.05	10.88	-10.81	J00202580+0049350	0.0176	10.84	-10.57	0.24	SE2	0.50
LCK-178064	10h46m48.^{s}3+56d34m04s	0.0450	12.24	3.21 ± 0.02	1.93 ± 0.04	11.15	-11.23	J01093517+0020132	0.0447	11.05	< -11.58	< -0.35	SE2	1.12
LCK-320371	10h38m32.^{s}4+57d24m01s	0.0471	12.79	4.86 ± 0.02	3.67 ± 0.05	10.96	-10.78	J01183556−0013594	0.0475	10.93	-10.03	0.75	SS2	1.06
LCK-523686	10h42m24.^{s}5+58d27m31s	0.0452	12.75	1.70 ± 0.02	0.65 ± 0.04	10.94	-11.38	J02110832−0039171	0.0199	10.98	-11.62	-0.24	SS1	0.56
LCK-415950	10h52m11.^{s}7+58d26m17s	0.0317	10.93	28.18 ± 0.02	100.16 ± 0.07	11.37	-10.49	J09374413+0245394	0.0230	11.46	-10.51	-0.02	SE1	0.68
LCK-086596	10h56m29.^{s}0+56d54m38s	0.0470	13.05	4.72 ± 0.03	1.04 ± 0.03	10.86	-10.93	J10205188+4831096	0.0531	10.88	-10.23	0.70	SE2	0.88
EN1-158103	16h07m36.^{s}6+53d57m31s	0.0298	12.48	19.97 ± 0.03	24.32 ± 0.04	10.70	-10.22	J10272950+0114490	0.0223	10.73	-10.17	0.05	SE2	0.65
EN1-360222	16h00m59.^{s}3+54d43m52s	0.0429	13.15	13.96 ± 0.02	16.53 ± 0.04	10.74	-10.10	J10435053+0645466	0.0273	10.83	-9.81	0.29	SS1	1.27
EN1-010947	16h11m9.^{s}8+53d09m47s	0.0367	12.99	0.79 ± 0.01	<0.30	10.67	< -11.63	J10435268+0645256	0.0273	10.73	-10.67	> 0.96	SS2	1.27
LCK-162208	10h44m38.^{s}2+56d22m11s	0.0240	10.96	39.40 ± 0.05	86.93 ± 0.05	11.12	-10.43	J10514450+5101303	0.0244	11.13	< -11.69	< -1.26	SE2	0.15
EN1-018834	16h10m47.^{s}6+53d25m21s	0.0631	13.17	1.92 ± 0.01	2.03 ± 0.03	11.06	-10.96	J12020424+5342317	0.0642	11.16	-10.75	0.21	SE2	0.87
LCK-233199	10h50m52.^{s}4+57d35m07s	0.0269	12.49	7.63 ± 0.02	8.64 ± 0.04	10.60	-10.65	J13082964+0422045	0.0241	10.53	-10.77	-0.12	SS1	1.29
LCK-019297	10h47m04.^{s}5+56d20m25s	0.0469	12.79	25.24 ± 0.01	48.28 ± 0.05	10.96	-9.89	J13325525−0301347	0.0472	10.90	-10.03	-0.13	SS2	0.79
LCK-703238	10h45m00.^{s}5+59d44m11s	0.0444	12.07	4.48 ± 0.03	2.00 ± 0.05	11.20	-11.21	J13325655−0301395	0.0472	11.21	-10.46	0.75	SS1	0.79
LCK-050667	10h49m55.^{s}9+56d49m50s	0.0457	12.84	1.92 ± 0.01	1.79 ± 0.05	10.92	-11.13	J13462001−0325407	0.0236	11.01	-10.99	0.14	SE1	1.28
LCK-027930	10h48m52.^{s}7+56d20m10s	0.0458	12.49	13.53 ± 0.02	12.10 ± 0.04	11.06	-10.43	J14005782+4251207	0.0327	11.01	-9.98	0.45	SS1	1.37
LCK-071868	10h54m09.^{s}3+56d49m15s	0.0466	12.82	22.30 ± 0.02	24.18 ± 0.05	10.94	-10.04	J14005882+4250427	0.0327	10.90	-9.70	0.34	SS2	1.37
EN1-516050	15h58m23.^{s}9+54d55m52s	0.0381	13.10	8.76 ± 0.02	7.92 ± 0.06	10.66	-10.38	J14250739+0313560	0.0359	10.66	-11.45	-1.08	SE2	1.31
LCK-641925	10h36m25.^{s}7+58d33m22s	0.0272	11.05	<1.89	<5.00	11.19	< -11.67	J14334683+4004512	0.0258	11.25	-10.46	> 1.22	SS1	1.22
LCK-400414	10h49m18.^{s}4+58d20m43s	0.0281	11.31	10.97 ± 0.03	6.04 ± 0.05	11.12	-11.11	J14334840+4005392	0.0258	11.10	-10.08	1.03	SS2	1.22
LCK-534543	10h44m45.^{s}1+58d27m17s	0.0314	11.48	30.42 ± 0.03	28.42 ± 0.06	11.14	-10.49	J15064391+0346364	0.0345	11.22	-11.54	-1.06	SS1	1.10
LCK-136060	11h00m54.^{s}4+57d46m32s	0.0483	12.56	2.26 ± 0.01	1.50 ± 0.04	11.08	-11.24	J15064579+0346214	0.0345	11.17	-10.37	0.87	SS2	1.10
LCK-172179	10h45m53.^{s}9+56d30m23s	0.0461	12.61	1.72 ± 0.01	3.11 ± 0.05	11.02	-11.14	J15101587+5810425	0.0312	11.02	-11.30	-0.15	SS1	0.53
LCK-564807	10h45m55.^{s}5+59d09m16s	0.0446	13.19	6.85 ± 0.02	5.91 ± 0.04	10.76	-10.46	J15101776+5810375	0.0312	10.79	-10.27	0.19	SS2	0.53
LCK-621286	10h33m19.^{s}8+58d04m33s	0.0454	11.83	2.09 ± 0.01	0.79 ± 0.04	11.32	-11.67	J15281276+4255474	0.0182	11.26	-10.62	1.05	SS1	1.32
LCK-038716	10h48m57.^{s}6+56d37m12s	0.0469	12.68	4.59 ± 0.02	4.16 ± 0.06	11.00	-10.82	J15281667+4256384	0.0182	11.03	-11.57	-0.75	SS2	1.32
LCK-582705	10h48m04.^{s}4+59d20m41s	0.0286	12.91	1.25 ± 0.02	1.09 ± 0.04	10.49	-11.32	J15562191+4757172	0.0195	10.49	-10.23	1.09	SE1	1.32
LCK-329416	10h40m26.^{s}2+57d26m23s	0.0472	12.53	7.23 ± 0.02	6.08 ± 0.05	11.07	-10.70	J16024254+4111499	0.0333	11.11	-9.92	0.78	SS1	0.64
LCK-040350	10h49m10.^{s}4+56d38m10s	0.0460	13.40	1.11 ± 0.01	4.00 ± 0.04	10.70	-10.89	J16024475+4111589	0.0333	10.78	-10.17	0.72	SS2	0.64
EN1-346329	16h02m45.^{s}0+54d32m01s	0.0636	13.42	4.67 ± 0.02	4.12 ± 0.04	10.97	-10.51	J17045089+3448530	0.0568	11.01	-9.98	0.52	SS2	0.63
LCK-182514	10h46m21.^{s}0+56d45m55s	0.0673	12.92	6.60 ± 0.02	5.14 ± 0.05	11.21	-10.57	J17045097+3449020	0.0568	11.28	-9.69	0.88	SS1	0.63
LCK-515902	10h41m39.^{s}9+58d19m02s	0.0723	12.69	2.30 ± 0.01	2.81 ± 0.05	11.37	-11.04	J20471908+0019150	0.0133	11.37	-10.90	0.14	SE1	0.99
LCK-347435	10h43m10.^{s}5+57d38m51s	0.0468	13.02	5.72 ± 0.01	6.79 ± 0.05	10.87	-10.54	J13153076+6207447	0.0306	10.91	-9.67	0.87	SS2	1.34
LCK-048281	10h50m10.^{s}8+56d43m37s	0.0481	12.62	2.57 ± 0.02	1.33 ± 0.05	11.05	-11.20	J13153506+6207287	0.0306	11.09	-9.21	1.99	SS1	1.34
NGC 0024	00h09m56.^{s}7-24d57m44s	0.0019	9.22	168.6 ± 3.8	125.2 ± 4.6	9.63	-10.72	J09494143+0037163	0.0063	9.71	-10.25	0.47	SS2	2.04
NGC 2403	07h36m51.^{s}4+65d36m09s	0.0004	6.45	5138.8 ± 622.9	5830.4 ± 53.2	9.99	-10.25	J09495263+0037043	0.0063	9.95	-10.11	0.14	SS1	2.04
NGC 0925	02h27m16.^{s}9+33d34m45s	0.0018	8.59	709.3 ± 79.8	827.4 ± 26.4	10.06	-10.27	J13082737+0422125	0.0241	10.15	-10.44	-0.17	SS2	1.29
NGC 3049	09h54m49.^{s}6+09d16m18s	0.0050	10.40	170.2 ± 3.0	434.2 ± 1.6	9.91	-10.01	J14530282+0317451	0.0052	9.92	-10.59	-0.58	SS2	1.42
NGC 3184	10h18m17.^{s}0+41d25m28s	0.0020	7.62	1733.2 ± 88.9	1437.8 ± 44.1	10.31	-10.33	J14530523+0319541	0.0052	10.17	-10.65	-0.31	SS1	1.42

Notes. Descriptions of columns: 1. Galaxy ID in the control sample; 2. R.A. (J2000) and decl. (J2000); 3. Redshift taken from SDSS; 4. K_s (K_{20}) magnitude taken from 2MASS; 5. IRAC 8 μm flux density (mJy) taken from DR2 of SWIRE survey; 6. MIPS 24 μm flux density (mJy) taken from DR2 of SWIRE survey; 7. Logarithm of the mass (in $M_\odot$); 8. Logarithm of the specific SFR (log(SFR/M)); 9. ID of the matched KPAIR galaxy; 10. Redshift of the KPAIR galaxy; 11. Logarithm of the mass (in $M_\odot$) of the KPAIR galaxy; 12. Logarithm of the specific SFR (log(SFR/M)) of the KPAIR galaxy; 13. SFR enhancement, $\epsilon = \log((\mathrm{SFR}/M)_{KPAIR-S}) - \log((\mathrm{SFR}/M)_{\mathrm{control}})$, of the KPAIR galaxy; 14. Category of the KPAIR galaxy. For example, "SE1" indicates that the galaxy is the primary of an S+E pair, and "SS2" denotes a secondary in an S+S pair; 15. Scale free separation parameter: SEP=$s/(r_1 + r_2)$, where s is the pair separation,r_1 the K-band Kron radius of the primary, and r_2 the K band Kron radius of the secondary.

mass bin. For those in S+S pairs, they have a similar trend as the total sample (Figure 5), showing a rather constant sSFR that is slightly above the mean of the total sample of paired spirals.

Figure 8 is a log(SFR/M)) versus log(M)) plot for individual non-AGN spirals in S+S and S+E pairs, compared to their counterparts in the control sample. All spirals in S+S pairs are detected. The upper limits for spirals in S+E pairs (two) and in the control sample (two) are shown by upside-down triangles and downward arrows, respectively. The two solid lines delineate the regions occupied by the LIRGs and ULIRGs. All three LIRGs are in S+S pairs, while there are no ULIRGs in any of the samples. The dot-dashed line marks the result of Brinchmann et al. (2004) for SDSS galaxies. It shows a very similar trend in the sSFR versus mass relation as that revealed by the data of single spirals in our control sample, although the SFR in Brinchmann et al. (2004) was derived using the optical emission lines data while it was derived using the IR luminosity in this work. The dashed line marks $\mathrm{SFR}/M = 1/t_{\mathrm{Hubble}}$, with the Hubble time $t_{\mathrm{Hubble}} = 13$ Gyr. Galaxies above this line have enhanced SFRs compared to a constant SFR over the Hubble time. There is indeed an excess of galaxies in S+S pairs above this line, while none of the spirals in S+E pairs has enhanced SFR.

We define a star formation enhancement indicator, ϵ, for each non-AGN spiral in KPAIR:

$$\epsilon = \log((\mathrm{SFR}/M)_{\mathrm{KPAIR\text{-}S}}) - \log((\mathrm{SFR}/M)_{\mathrm{control}}), \quad (4)$$

where $(\mathrm{SFR}/M)_{\mathrm{KPAIR\text{-}S}}$ and $(\mathrm{SFR}/M)_{\mathrm{control}})$ are the sSFR of the paired galaxy and that of its match in the control sample, respectively.

Figure 9 is a plot of means of ϵ in the log(M) bins. For the S+S subsample, there is a clear mass dependence of ϵ, which can be expressed by its linear regression:

$$\langle\epsilon\rangle_{\mathrm{S+S}} = 0.03(\pm 0.14) + 0.47(\pm 0.15) \times \log\left(\frac{M}{10^{10} \times M_\odot}\right). \quad (5)$$

This relation is confined to the mass range covered by our samples: $10.0 \lesssim \log(M/M_\odot) \lesssim 11.5$. For the S+E subsample, the mean ϵ is consistent with 0 in all mass bins.

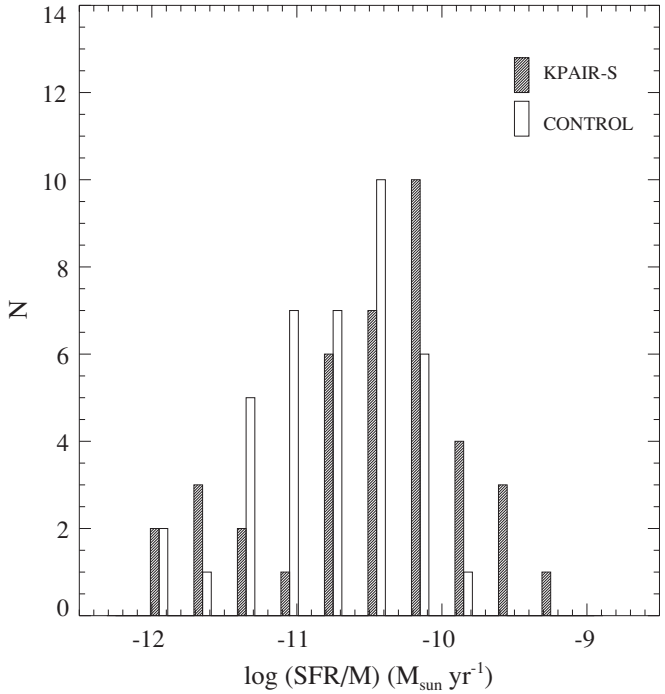

Figure 4. Histograms of log(SFR/M)) distributions of the non-AGN spirals in the KPAIR sample ("KPAIR-S") and of the control sample.

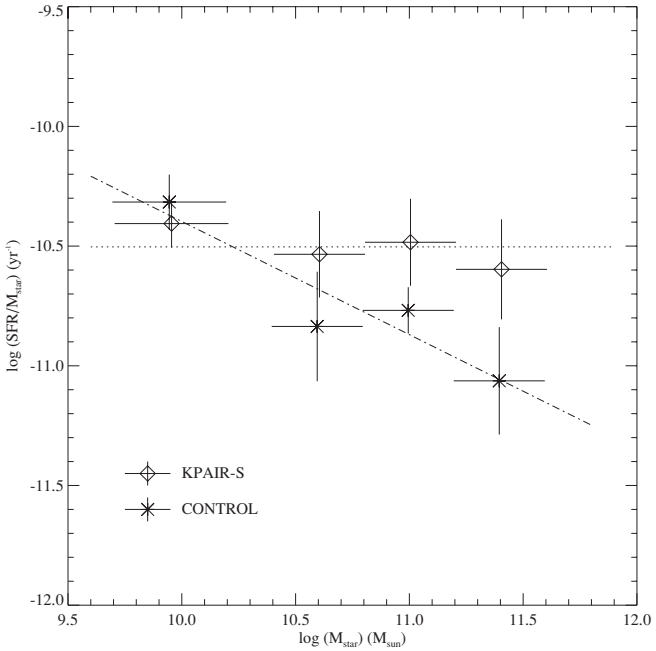

Figure 5. Comparison of means of log(SFR/M) of paired and single spirals in mass bins. The dotted line marks the mean SFR/M of non-AGN spirals in KPAIR, and the dot-dashed line marks the linear regression of those in the control sample.

There is a known dependence of sSFR on local environment in the sense that galaxies in higher local-density environments tend to have lower sSFR (Kauffmann et al. 2004). Could the difference in the SFR/M of spirals in S+S pairs and in S+E pairs be due to different mean local densities of the two types of pairs? If S+E pairs are preferentially found in the denser environment, then the lower SFR/M of the spirals in these pairs compared to those in S+S pairs is just another consequence of the SFR–environment relation. We made the following test for this hypothesis. Figure 10 shows the selection function of the parent sample of KPAIR sample (Section 2). In the plot, dots are the 59,312 DR3/2MASS galaxies in the parent sample, and eight-point stars are the non-AGN spirals in the KPAIR sample. The highest redshift of paired spirals is at $z \sim 0.06$, corresponding to a limiting mass of $M_{\rm limit} = 10^{10.9}\ M_{\odot}$. Adopting this limiting mass, around each non-AGN spirals in the KPAIR sample we counted neighbors within the parent sample using the following criteria: (1) $M \geqslant M_{\rm limit}$; (2) distance $\leqslant$ 2 Mpc; and (3) $\delta V_z \leqslant 1000$ km s^{-1}. In Figure 11, means of the neighbor counts ($N_{\rm neighbor}$) around spirals in S+S pairs and in S+E pairs in the individual mass bins are compared with each other. According to Figure 11, there is no evidence for the spirals in S+E pairs having systematically higher local density than those in S+S pairs. Therefore, the difference in the SFR/M of

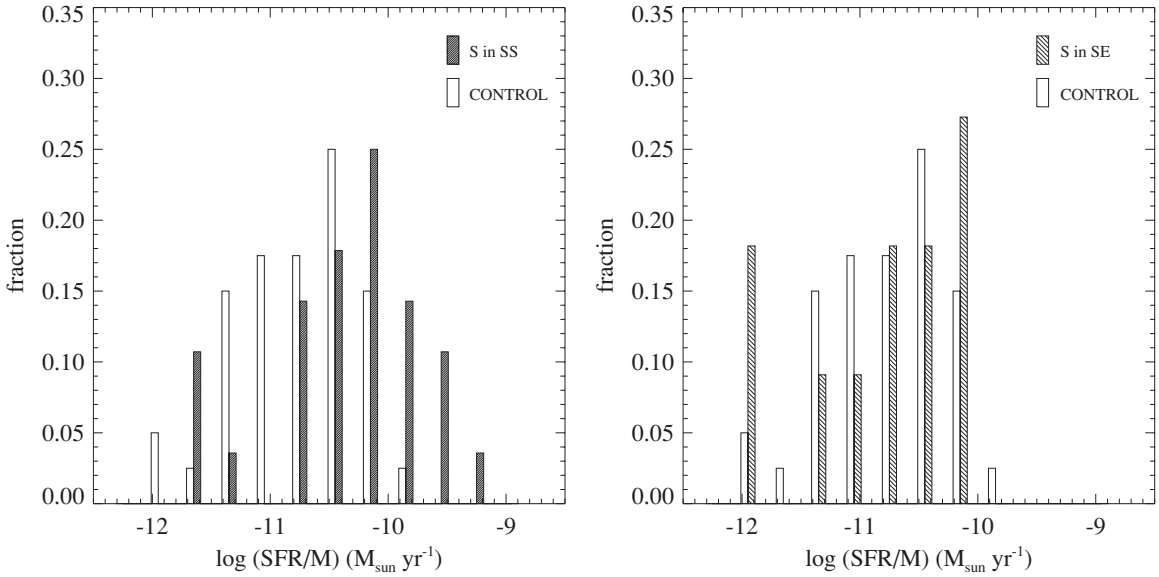

Figure 6. Left: histograms of log(SFR/M)) distributions of the non-AGN spirals in S+S pairs (28 galaxies) and of the control sample. Right: histograms of log(SFR/M)) distributions of the non-AGN spirals in S+E pairs (11 galaxies) and of the control sample.

Table 5
Mean Specific Star Formation Rate (SFR/M) in Mass Bins

Mass Bin ($M_\odot$)	Mean log(SFR/M) (yr^{-1})			
	KPAIR-S	CONTROL	S in S+S	S in S+E
$9.7 < \log(M) < 10.2$	-10.41 ± 0.10 (5)	-10.32 ± 0.11 (5)	-10.41 ± 0.10 (5)	
$10.4 < \log(M) < 10.8$	-10.53 ± 0.18 (7)	-10.84 ± 0.23 (7)	-10.47 ± 0.15 (4)	-10.62 ± 0.42 (3)
$10.8 < \log(M) < 11.2$	-10.48 ± 0.18 (20)	-10.77 ± 0.10 (20)	-10.23 ± 0.20 (14)	-11.07 ± 0.29 (6)
$11.2 < \log(M) < 11.6$	-10.60 ± 0.21 (7)	-11.06 ± 0.22 (7)	-10.55 ± 0.30 (5)	-10.70 ± 0.19 (2)

spirals in the two different types of pairs is not due to the local-density dependence. Interestingly, in Figure 11, there is a clear indication for the density/mass correlation, consistent with the literature (Kauffmann et al. 2004).

5.5. Comparison of Primaries and Secondaries in KPAIR

Previous studies (Ellison et al. 2008; Woods & Geller 2007) have found that the secondaries in minor-merger pairs (mass ratio > 3) have higher SFR enhancement than the primaries. We checked whether this is also true for spirals in KPAIR, which includes only major-merger pairs. The answer is negative. As shown in Figure 12, there is no significant difference between the mean SFR/M of primaries and that of secondaries in any mass bins studied in this work. The K–S test finds a 62% probability for the null hypothesis that SFR/M distributions of the primaries and of the secondaries are drawn from the same population.

5.6. Enhancement in One or Two Components?

In an early IR study of interacting pairs, Joseph et al. (1984) found that among all the 22 pairs for which they obtained $K-L$ colors for both components, only one component of each pair exhibited $K-L$ excess. They interpreted the result as evidence for single-component star formation enhancement in interacting pairs. Contrarily, in an *IRAS* study of isolated pairs, Xu & Sulentic (1991) argued that they saw indications of IR enhancement in both components in the close-interacting (CLO) S+S pairs, though their results were not conclusive because most of their CLO pairs are unresolved by *IRAS*. With the much improved angular resolution of *Spitzer* which resolved all pairs in the KPAIR sample, we can address directly the question whether the SFR is enhanced in only one component or in both components in close-interacting S+S pairs.

Given our result that only more massive galaxies in S+S pairs have SFR/M enhancement (Figures 7 and 9), we picked the 10 pairs (out of 15 in total) whose two components are both non-AGN and more massive than $10^{10.7}\ M_\odot$. Figure 13 is an SFR/M plot of individual pairs, each pair in a separate column, showing the log(SFR/M) values of both components as well as of their counterparts in the control sample. The pairs are sorted according to the log(SFR/M) of the IR-brighter component.

The results in Figure 13 can be summarized as the following:

1. Massive galaxies ($M \geqslant 10^{10.7}\ M_\odot$) in close major-merger S+S pairs have very diversified star formation activity levels, from very quiescent (similar to "red and dead" galaxies) to strong starburst (e.g., in LIRGs).
2. In individual pairs, the SFR/M values of the two components show a certain level of concordance ("Holmberg effect"): when one component has a strong star formation enhancement, the other is usually enhanced as well (with only one exception: pair No. 7 = J1043+0645). On the other hand, if one component is a "red and dead" galaxy, the other one usually shows no sign of star formation enhancement, either.[10]

Figure 14 confirms the "Holmberg effect" between the SFR/M of the two pair components. The values of log(SFR/M) of the two components are highly correlated, with the Spearman's rank correlation coefficient equal to 0.58 and the probability for the null hypothesis being only 0.08. On the other hand, no correlation is found between log(SFR/M) values of their matches in the control sample, as is expected.

Result (2) is apparently in contradiction with that of Joseph et al. (1984). This might be explained by the differences between our study and that of Joseph et al. (1984). Several pairs in the sample of Joseph et al. (1984) belong to the category of minor mergers (e.g., Arp 283 and Arp 294), for which indeed only one component (the secondary) is usually enhanced (Woods & Geller 2007). Furthermore, the study of Joseph et al. (1984) was confined to the nuclei of the interacting galaxies, and the $K-L$ excess is only sensitive to very hot dust emission from compact starbursts. It is possible that these compact nuclear starbursts have shorter timescales, and therefore significantly lower chance to occur simultaneously in both components, compared to the star formation enhancement over entire galaxy bodies as probed by our *Spitzer* observations.

Figure 15 is a plot of log(SFR/M) versus neighbor counts ($N_{\rm neighbor}$, as defined in Section 5.4) for the same paired galaxies plotted in Figure 13. There is no discernible dependence of log(SFR/M) on $N_{\rm neighbor}$ in the plot. Therefore, it is something other than the local density that determines whether the two galaxies in an S+S pair should or should not have enhanced star formation activity.

5.7. Separation and SFR/M Enhancement

Previous studies (Xu & Sulentic 1991; Barton et al. 2000; Lambas et al. 2003; Nikolic et al. 2004; Alonso et al. 2004; Woods et al. 2006; Barton et al. 2007; Ellison et al. 2008) found that the star formation enhancement in pairs of separation $\lesssim 20\ h^{-1}$ kpc is much stronger than those of larger separations. Using our sample, we can address the question whether there is still dependence of the SFR on separation for pairs within this separation limit. We define a normalized separation parameter:

$$\mathrm{SEP} = \frac{s}{r_1 + r_2}, \tag{6}$$

where s is the projected separation, and r_1 and r_2 are the K-band Kron radii (taken from 2MASS) of the primary and the secondary, respectively, in the same units as those of s (kpc or arcsec). In the ideal case of a pair of two round galaxies, the two component galaxies overlap with each other when SEP < 1.

Figure 16 is a histogram of SEP distribution of non-AGN spirals in KPAIR. The median is at SEP ~ 1 (mean SEP =

[10] This is in agreement with the lack of SFR/M enhancement for spirals in S+E pairs.

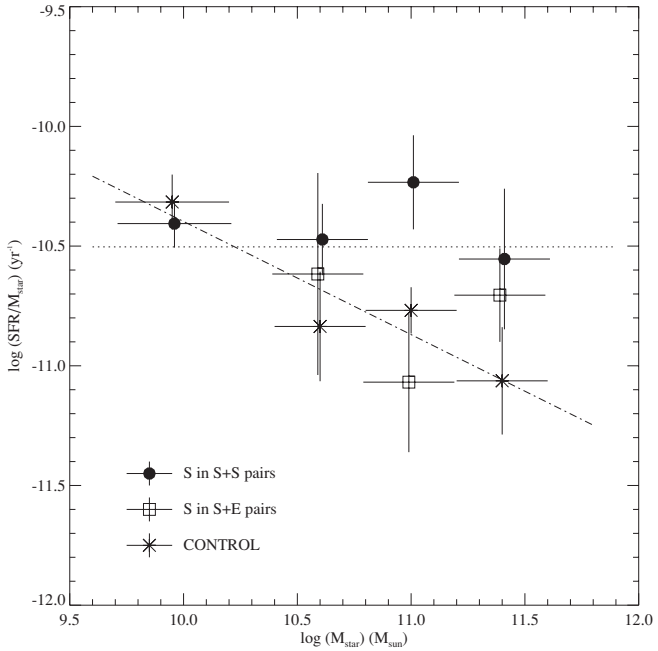

Figure 7. Comparison of means of log(SFR/M) of spirals in S+S pairs, in S+E pairs, and in the control sample. The dotted line marks the mean log(SFR/M) of all non-AGN spirals in KPAIR, and the dot-dashed line marks the linear regression of those in the control sample.

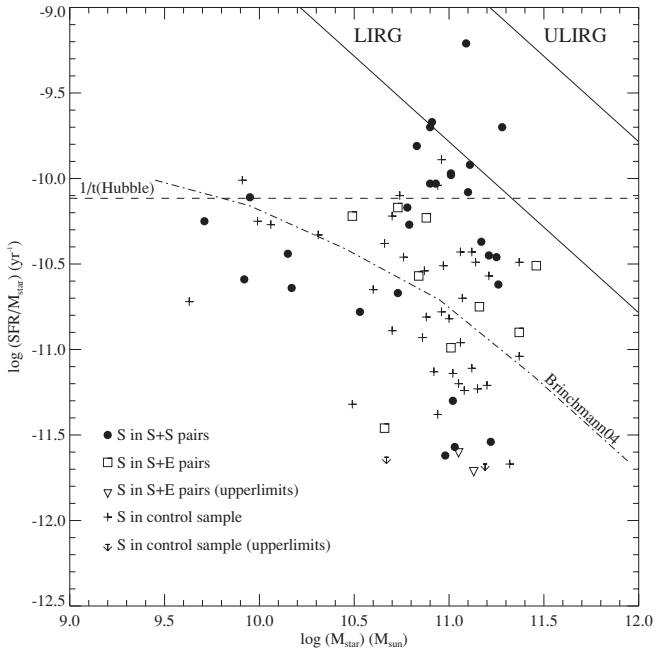

Figure 8. sSFR (SFR/M) vs. mass plot for the non-AGN spirals in pairs and those in the control sample. The dashed line marks SFR/$M = 1/t_{\rm Hubble}$, with the Hubble time $t_{\rm Hubble} = 13$ Gyr. The dot-dashed line is the result of Brinchmann et al. (2004) for SDSS galaxies, corrected for the IMF and the Hubble constant differences (the Kroupa IMF and $H_0 = 70$ (km s^{-1} Mpc^{-1}) in Brinchmann et al. 2004; the Salpeter IMF and $H_0 = 75$ (km s^{-1} Mpc^{-1}) in this work).

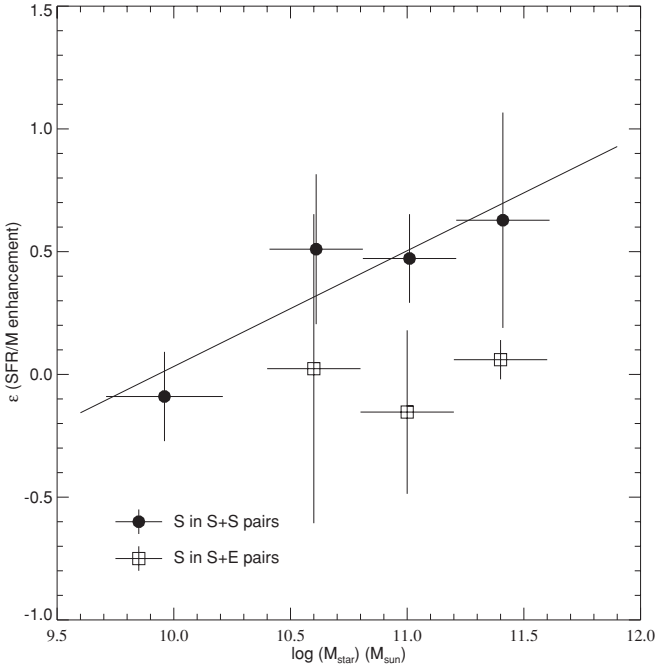

Figure 9. Plot of means of SFR/M enhancement, $\epsilon = \log((\mathrm{SFR}/M)_{\rm KPAIR\text{-}S}) - \log((\mathrm{SFR}/M)_{\rm control})$, in the log($M$) bins. The solid line is the linear regression of the log(M) dependence of ϵ of spirals in S+S pairs: $\langle\epsilon\rangle_{\rm S+S} = 0.03 + 0.47 \times \log[M/(10^{10} \times M_{\odot})]$.

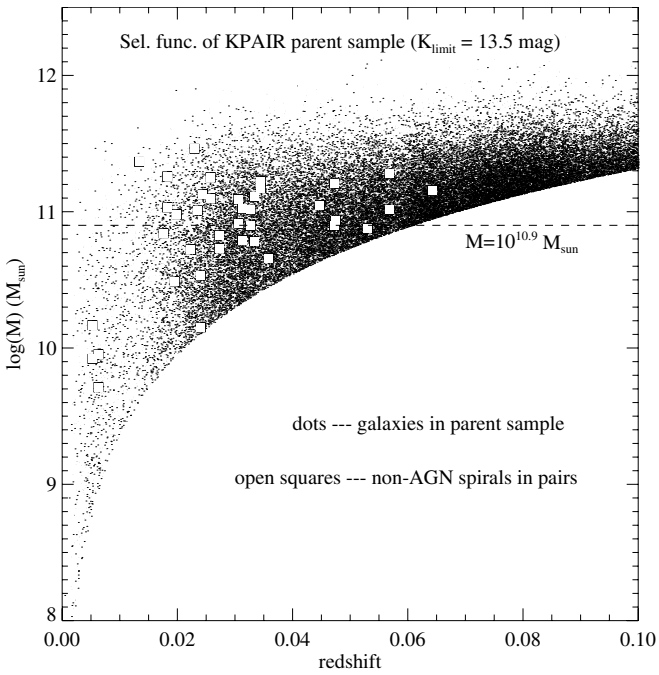

Figure 10. Selection function of the parent sample of the KPAIR sample. Symbols: dots are galaxies in the parent sample, eight-point stars are the non-AGN spirals in the KPAIR sample. The dashed line marks the limiting mass ($10^{10.9}$ $M_{\odot}$) for the neighbor selection.

1.05 ± 0.40). Figure 17 is a plot of mean log(SFR/M) versus log(M) of spirals in S+S pairs, separated into two subsamples of SEP < 1 and SEP $\geqslant 1$. For both subsamples, the log(SFR/M) versus log(M) relation scatters around the mean of the total sample without any obvious trend, and no significant difference between the two subsamples is detected. This seems to suggest that the separation is not an important parameter any more once the two galaxies are close enough. There might be several conflicting factors affecting the star formation activity versus SEP relation in close major-merger pairs. On the one hand, colliding pairs with SEP < 1 may undergo collisionally triggered starbursts in the regions where the two galaxies overlap, as in the case of the Antennae Galaxies (Xu et al. 2001). On the other hand, Gao & Solomon (1999) found a correla-

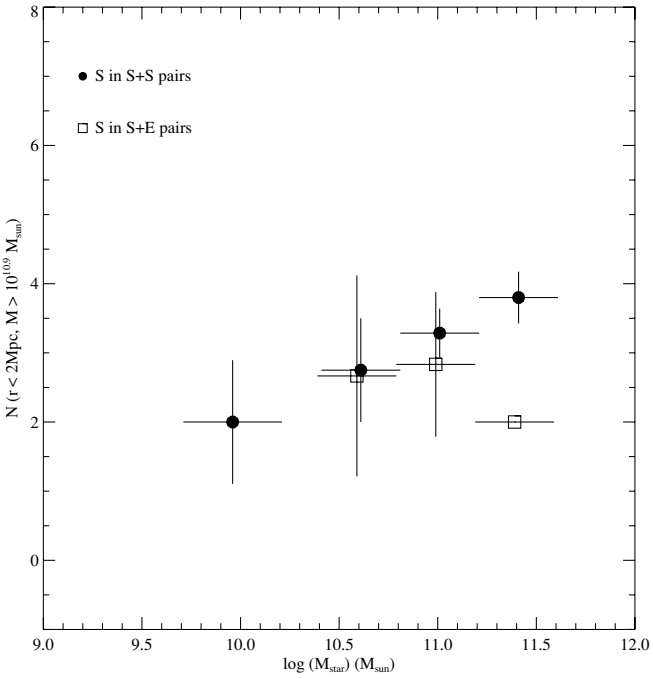

Figure 11. Mean neighbor counts in individual mass bins. Filled circles: results of non-AGN spirals in S+S pairs. Open squares: results of non-AGN spirals in S+E pairs. Horizontal error bars show the bin width of the mass bins. Vertical error bars present the standard deviations of the means. No vertical error bar is plotted for the last data point of the S+E subsample because there is only one galaxy in the corresponding mass bin.

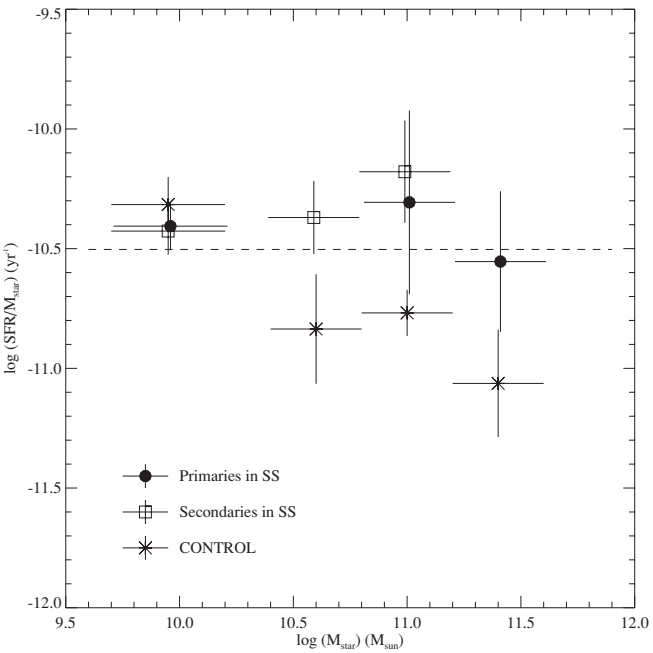

Figure 12. Average sSFRs of primaries and secondaries in KPAIR pairs. The mass bins are the same as in Figure 5. The dotted line marks the mean SFR/M of the KPAIR-S sample.

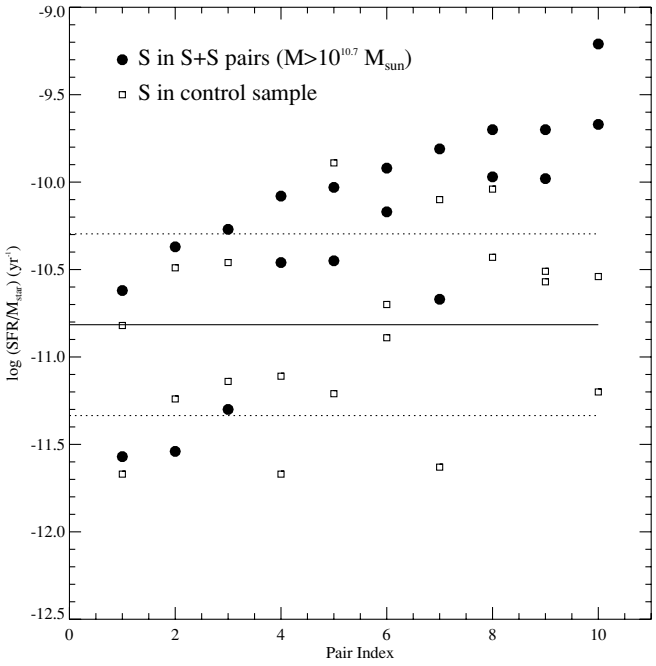

Figure 13. log(SFR/M) plot of 10 S+S pairs with $M \geqslant 10^{10.7}\ M_{\odot}$. Filled circles represent paired galaxies, and open squares represent their counterparts in the control sample. Pairs are arranged according to the log(SFR/M) value that is the higher one among the two. The solid line and the dotted lines mark the mean log(SFR/M) and the $\pm 1\sigma$ boundaries, respectively, with the mean and the σ (rms) derived using the 20 control galaxies included in this plot.

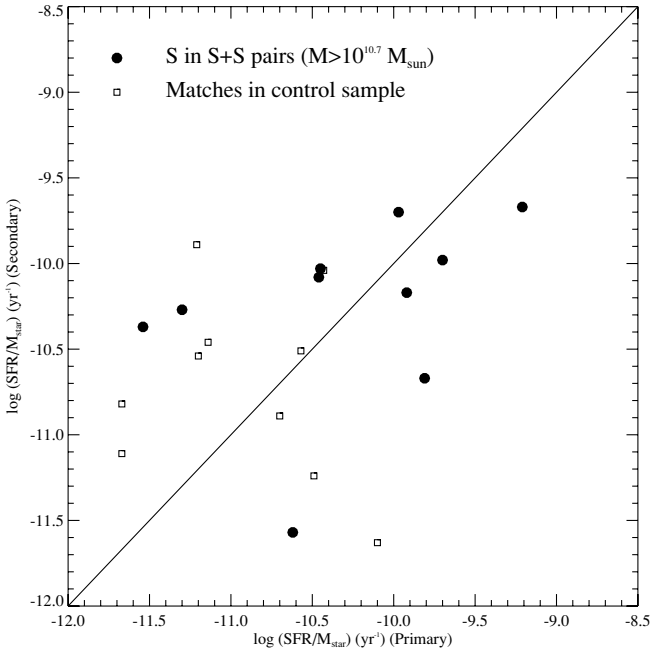

Figure 14. Correlation plot of log(SFR/M) of two components in the S+S pairs in Figure 13. Filled circles represent the pairs, and open squares represent their counterparts in the control sample.

tion between molecular gas content and the pair separation, suggesting a progressive gas depletion due to prolonged star formation activity. It should also be noticed that SEP is derived from the projection of the real, three-dimensional separation. Any dependence on the true separation can be significantly disturbed by the projection effect.

5.8. Contribution of KPAIR Galaxies to the Cosmic SFR Density

In this subsection, we estimate the contribution of galaxies in close major-merger pairs, as defined by the pair selection criteria in Section 2, to the total cosmic SFR density in the local universe. Assuming the contribution for E galaxies is negligible,

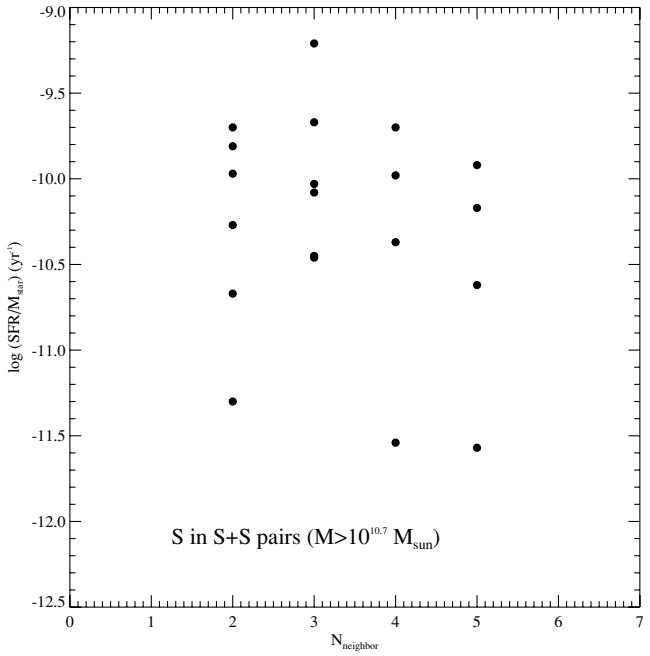

Figure 15. Plot of log(SFR/M) vs. neighbor counts for the same paired galaxies plotted in Figure 13.

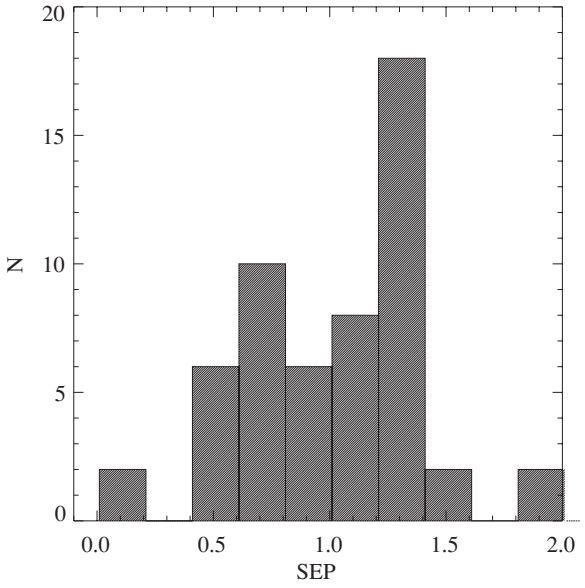

Figure 16. Histogram of the SEP distribution of non-AGN spirals in the KPAIR sample.

this can be estimated as follows:

$$\dot{\rho}_{\rm KPAIR} = \int (SFR/M)_{KPAIR\text{-}S} \times \psi(M) \times f_s \times M \times dM, \quad (7)$$

where $\psi(M)$ is the mass function of KPAIR galaxies and f_s the S fraction (N_S/N). Because the mass dependence of $(\mathrm{SFR}/M)_{\rm KPAIR\text{-}S}$ is rather flat, we assume it is constant and equal to the mean SFR/M of the KPAIR-S sample: $(\mathrm{SFR}/M)_{\rm KPAIR\text{-}S} = 10^{-10.50}\,\mathrm{yr}^{-1}$. The mass function ψ and the S fraction f_s are taken from Domingue et al. (2009). The result of the integration is $\dot{\rho}_{\rm KPAIR} = 2.54 \times 10^{-4} M_\odot\ yr^{-1}\ Mpc^{-3}$, which is 1.7% of total cosmic SFR density in the local universe ($\rho_\cdot = 0.015\,M_\odot\ \mathrm{yr}^{-1}\ \mathrm{Mpc}^{-3}$; Yun et al. 2001).

It should be pointed out that, because of the criterion on pair separation ($r \geqslant 5\ h^{-1}$ kpc), mergers already coalesced are

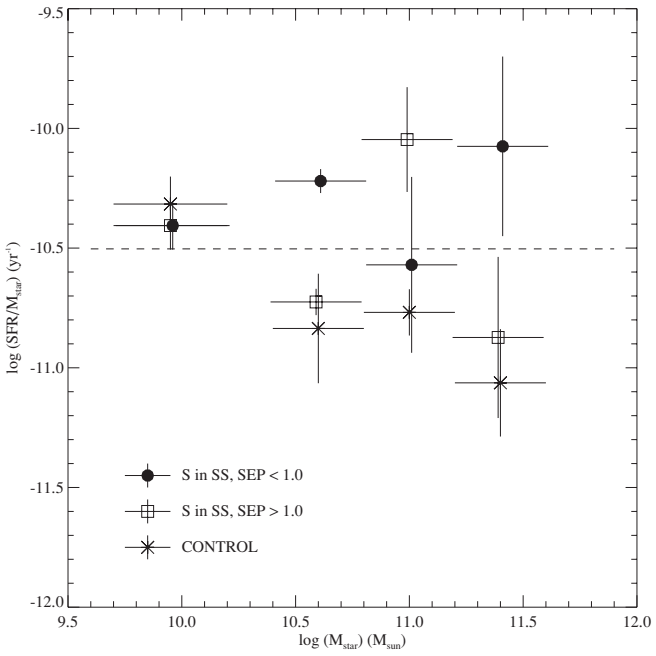

Figure 17. Average sSFRs of non-AGN spirals in S+S pairs, separated into two subsamples of SEP < 1 and SEP $\geqslant 1$, respectively. The mass bins are the same as in Figure 5. The dotted line marks the mean SFR/M of the non-AGN spirals in the KPAIR sample.

missing in the KPAIR sample. This population includes the majority of ULIRGs and many LIRGs. Assuming that all ULIRGs and 70% LIRGs are coalesced mergers, and estimating their densities using the IR LF of Yun et al. (2001), we found that the total SFR in these sources is $\dot{\rho} = 2.77 \times 10^{-4}\,(M_\odot\ yr^{-1}\ Mpc^{-3})$, i.e., nearly the same as that in the KPAIR galaxies. Therefore, in the $z = 0$ universe, the total SFR in close major mergers is $\dot{\rho} = 5.31 \times 10^{-4}\,(M_\odot\ yr^{-1}\ Mpc^{-3})$. This is only 3.5% of the local cosmic SFR density, a truly negligible contribution indeed.

6. DISCUSSION

6.1. Dependence of SFR Enhancement on Companion's Morphological Type

The star formation enhancement found in interacting galaxies is often explained in terms of gas inflow caused by gravitational torques of interaction-induced bars (Hernquist & Barnes 1991; Barnes & Hernquist 1996). However, this theory cannot explain our result that the star formation enhancement depends on the morphological type of the companion galaxy: while spirals in S+S pairs show significant enhancement, those in S+E pairs have star formation activity comparable to that of single spirals. It appears that, in addition to pure gravitational effects, some other factors related to the companion must play important roles in the interaction-induced star formation.

A related result was reported by Park & Choi (2009) in a study of the dependence of physical parameters of SDSS galaxies on small-scale and large-scale environments. These authors found that the SFR of late-type galaxies is enhanced when the nearest neighbor is also a late type, but reduced when the neighbor is an early type. They suggested that the hot gas halo of an early-type companion can suppress the SFR of a late-type galaxy, through hydrodynamic effects such as ram pressure stripping, viscous stripping, and thermal evaporation, analogous to what is being encountered by late-type galaxies in clusters (Boselli &

Gavazzi 2006). This interpretation can be applied to our result of low sSFR enhancement of spirals in the S+E pairs. Verdes-Montenegro et al. (2001) argued that a similar mechanism might be responsible for the depressed SFR of galaxies in compact groups (but see Rasmussen et al. 2008). The X-ray observations of four S+E pairs by Grützbauch et al. (2007) indeed showed evidence for extended X-ray halos in the E components, lending support to this hypothesis.

It should be noticed, however, that our result of no SFR enhancement for spirals in S+E pairs is based on a small sample of 11 S+E pairs, and therefore should be confirmed by future studies using larger samples. Furthermore, there are known exceptions of strong starbursts in S+E pairs in the literature, such as NGC 3561A (a LIRG) in Arp 105 (Duc et al. 1997). It will be worthwhile to investigate why galaxies like NGC 3561A behave differently. One noticeable feature of NGC 3561A is the segregation of atomic and molecular gas: the H I gas is completely displaced out of the disk, and the nuclear starburst is supported by pure molecular gas (Duc et al. 1997). Another spiral galaxy in an S+E pair that has a similar atomic–molecular gas segregation is NGC 1144 in Arp 118 ("Yin-Yang Galaxy;" Appleton et al. 2003), also an LIRG, though in this case the nucleus is an AGN rather than a starburst.

6.2. "Holmberg Effect"

The "Holmberg effect" on SFR/M of massive S+S pairs (Figure 14) is in agreement with the result of Kennicutt et al. (1987) derived from the integrated H_α fluxes, and that of Hernández-Toledo & Puerari (2001) based on the $(B-V)$ colors. Apparently, the effect is present in star formation indicators of very different timescales ($\sim 10^7$ yr for the H_α emission, $\sim 10^8$ yr for the IR emission, and $\sim 10^9$ yr for the $(B-V)$ color). On the other hand, it has been found only in global star formation indicators for entire galaxies, but not in those for the nuclear star formation activity (Joseph et al. 1984). Interestingly, the SFR dependence on interaction parameters has been invoked to explain both the presence of the correlation between the SFR of the two components (Kennicutt et al. 1987), and the absence of it (Joseph et al. 1984). However, we have shown that for spirals in close major-merger pairs, interaction parameters such as the separation are not important factors in determining whether a galaxy has enhanced SFR/M or not (Figure 17). It is possible that the concordant star formation behavior of galaxies in a close major-merger pair is dictated by the local environment within/around the DMH surrounding the pair. But, as shown in Figure 15, the level of star formation activity of these pairs depends very little on the local density. It is possible that the SFR is suppressed in those quiescent S+S pairs because there is diffuse hot intergalactic medium (IGM) gas in the DMH, in a similar way as what may be happening in the S+E pairs (see Section 6.1). Or, in a related scenario, it might be because the DMHs of these quiescent S+S pairs have no "cold streams" of IGM gas (Keres et al. 2009) to fuel the star formation in the component galaxies. It will be worthwhile to confirm or refute these speculations in future studies.

6.3. Dependence of SFR Enhancement on Mass

Our result indicating a lack of SFR enhancement in low-mass late-type interacting galaxies is in agreement with observations of Brosch et al. (2004) and Telles & Maddox (2000). In the theory proposed by Mihos et al. (1997), this is due to the fact that these galaxies do not have sufficient disk self-gravity to amplify dynamical instabilities, and this disk stability in turn inhibits interaction-driven gas inflow and starburst activity.

On the other hand, studies including minor mergers (Woods & Geller 2007; Ellison et al. 2008; Li et al. 2008) found significant SFR enhancement in low-mass ($M \lesssim 10^{10}\,M_\odot$) interacting galaxies. It appears that, in a minor-merger pair, a low-mass galaxy can have much stronger SFR enhancement when its companion is much more massive (Woods & Geller 2007).

6.4. Overall SFR Enhancement in Major-merger Pairs

We have found that, for close major mergers, only massive ($M \gtrsim 10^{10.5}\,M_\odot$) galaxies in S+S pairs have significant star formation enhancement. These galaxies are less than 30% in a K-band selected sample of close major mergers (Domingue et al. 2009), and yet some of them are locked in low sSFR pairs (Figure 13). Therefore, even for spiral galaxies in close major-merger pairs which harbor most merger-induced starbursts in the universe, the star formation enhancement due to galaxy–galaxy interaction is still confined to a small sub-population. This is consistent with the observations of Bergvall et al. (2003) and the simulations of Di Matteo et al. (2008), both argued that mergers are not very efficient in triggering significantly enhanced star formation. This is also consistent with the low contribution of major-merger galaxies to the cosmic SFR density in the local universe (Section 5.8) and in the universe of intermediate redshift ($z \sim 0.24$–0.80; Jogee et al. 2009).

7. SUMMARY

We present *Spitzer* observations for a sample of close major-merger pairs of galaxies, selected from 2MASS/SDSS-DR3 cross-matches. The scientific goals are (1) studying the star formation activity in these galaxies and (2) setting a local bench mark for the cosmic evolution of close major mergers. The *Spitzer* KPAIR sample (27 pairs, 54 galaxies) includes all spectroscopically confirmed spiral–spiral (S+S) pairs and spiral–elliptical (S+E) pairs in a parent sample that is complete for primaries brighter than $K = 12.5$ mag, projected separations of $5\ h^{-1}$ kpc $\leqslant s \leqslant 20\ h^{-1}$ kpc, and mass ratios $\leqslant 2.5$. There are 42 spiral galaxies and 12 elliptical galaxies in the sample. These galaxies harbor six known AGNs, three in spirals and three in ellipticals.

Spitzer observations include images in the four IRAC bands at 3.6, 4.5, 5.8, and 8.0 μm, and the three MIPS bands at 24, 70, and 160 μm. They show very diversified IR emission properties among KPAIR galaxies. Among the paired spirals, the majority have rather moderate IR luminosity ($\sim 10^{10}\,L_\odot$). There are four LIRGs ($\sim 10\%$ of KPAIR-S subsample), but no ULIRGs. The SFR, estimated using the IR luminosity, and the sSFR of non-AGN spirals (39 of them) in KPAIR are compared to those of single spirals in a control sample. Each of the 39 galaxies in the control sample matches a non-AGN spiral in KPAIR with the same mass (estimated from the K-band luminosity). The following results are found.

1. The mean SFR of non-AGN spirals in the KPAIR sample (KPAIR-S) is significantly enhanced compared to that of the single spirals in the control sample. The means of log(SFR) of the KPAIR-S galaxies and of the galaxies in the control sample are 0.36 ± 0.12 and 0.07 ± 0.08, respectively. And the means of log(SFR/M) of the KPAIR-S galaxies and of the galaxies in the control sample are -10.50 ± 0.10 and -10.78 ± 0.08, respectively. The K–S test rejects at the

96.1% confidence level the null hypotheses that the two samples are drawn from the same population.

2. When separating the non-AGN paired spirals into those in S+S pairs (28) and in S+E pairs (11), only the former show SFR/M enhancement whereas the latter do not. The means of log(SFR/M) of the spirals in S+S pairs and of those in S+E pairs are -10.36 ± 0.11 and -10.88 ± 0.19, respectively.
3. The SFR/M enhancement of spirals in S+S pairs is highly mass dependent: only those with $M \geqslant 10^{10.5}\ M_{\odot}$ show significant enhancement, whereas relatively low-mass ($M \sim 10^{10}\ M_{\odot}$) spirals in S+S pairs have about the same SFR/M as their counterparts in the control sample.
4. We define ϵ as the SFR enhancement parameter, $\epsilon = \log((\mathrm{SFR}/M)_{\mathrm{KPAIR\text{-}S}}) - \log((\mathrm{SFR}/M)_{\mathrm{control}})$, where $(\mathrm{SFR}/M)_{\mathrm{KPAIR\text{-}S}}$ and $(\mathrm{SFR}/M)_{\mathrm{control}}$ are the SFR/M of a paired spiral and that of its match in the control sample, respectively. For spirals in the S+S subsample, there is a strong linear dependence of ϵ on log(M), specified as $\langle\epsilon\rangle_{\mathrm{S+S}} = 0.03(\pm0.14) + 0.47(\pm0.15) \times (\log(M/10^{10}\ M_{\odot}))$. The relation is valid for the mass range of $10.0 \lesssim \log(M/M_{\odot}) \lesssim 11.5$.
5. For spirals in the KPAIR sample, which includes only close major mergers, there is no systematic difference between the log(SFR/M) of spirals with SEP < 1 and those with SEP $\geqslant 1$, SEP being the normalized separation parameter (SEP $= s/(r_1 + r_2)$). Also, there is no significant difference between the means of log(SFR/M) for the primaries and the secondaries.
6. There is evidence for a correlation between the global star formation activities (but not the nuclear activities) of the component galaxies in massive S+S major-merger pairs (the "Holmberg effect").
7. The contribution of KPAIR galaxies to the cosmic SFR in the local universe is $\dot{\rho}_{\mathrm{KPAIR}} = 2.54 \times 10^{-3}\ M_{\odot}\ \mathrm{yr}^{-1}\ \mathrm{Mpc}^{-3}$. This is 1.7% of total cosmic SFR density in the local universe. Adding the SFR in mergers already coalesced, which are missed by the KPAIR sample and may include many ULIRGs and LIRGs, the total SFR in close major mergers is $\dot{\rho} = 5.31 \times 10^{-3}\ M_{\odot}\ \mathrm{yr}^{-1}\ \mathrm{Mpc}^{-3}$. This is only 3.5% of the local cosmic SFR density.

C.K.X. thanks David Shupe for useful discussions on the SWIRE data handling. Y.G.'s research is partly supported by grants 10833006 and 10621303 of NSF of China. W.-H.S. and Y.-W.C. acknowledge the support of the National Science Council in Taiwan under the grant NSC 97-2112-M-002-014. Constructive comments by an anonymous referee are acknowledged. This work is based on observations made with the *Spitzer Space Telescope*, which is operated by the Jet Propulsion Laboratory, California Institute of Technology under a contract with NASA. Support for this work was provided by NASA. This research has made use of the NASA/IPAC Extragalactic Database (NED), which is operated by the Jet Propulsion Laboratory, California Institute of Technology, under contract with the National Aeronautics and Space Administration.

APPENDIX A

NOTES ON INDIVIDUAL PAIRS

J0020+0049. The FIR emission of this S+E pair is dominated by the S component. The E component was only barely detected in the MIPS 24 μm band, and undetected in the 70 and 160 μm bands.

J0109+0020. Neither galaxy in this S+E pair is detected in any of the MIPS bands, a unique case in the sample. The S component shows an arm-like feature in the optical images, but was classified as an E galaxy by the automatic classification routine based on the optical color and light concentration. Apparently it is a "red and dead" galaxy, perhaps of early S type.

J0118–0013. Both components of the S+S pair are well detected by IRAC and MIPS. The western component has a narrow-line AGN (Hao et al. 2005). In its optical image, there is a blue, jet-like feature pointing to the companion galaxy. It is an LIRG, with $\log L_{\mathrm{TIR}}/L_{\odot} = 11.41$, dominating the total dust emission of the pair. From aperture photometry of the IRAC bands, the AGN contributes $\sim 40\%$ of the dust emission of the galaxy. The eastern component looks like a normal late-type spiral, contributing only $\sim 12\%$ of the L_{TIR} of the pair.

J0211–0039. This S+S pair is KPG 058 (Karachentsev 1972). Both galaxies are seen edge-on. The western component (an Sbc galaxy) has a narrow-line AGN (Hao et al. 2005). It dominates the dust emission of the pair.

J0906+5144. Another KPG pair, KPG 185. The western component is classified as E type in our scheme, though according to NED it is an Sa galaxy. The eastern component is an S type with a narrow-line AGN (Hao et al. 2005). The IRAC 8 μm band image shows a nucleus+ring morphology, with most of the emission from the ring.

J0937+0245. This S+E pair is Arp 142 (= VV 316), classified as "ring galaxy" by RC2 (de Vaucouleurs et al. 1976). The S component (NGC 2936) is very disrupted. The optical/NIR morphology looks like a bird head, with the nucleus being the eye. The tidal tails, which form the "neck" of the bird, contain several star-forming regions bright in the IR (see the 8 and 24 μm image). However, most of the dust emission is still confined within the nucleus+disk (i.e. the bird head) region. The E component (NGC 2937) is undetected in the 70 and 160 μm bands.

J0949+0037. This S+S pair is KPG 216. It is one of the three pairs in our sample larger than 2.′5. The two relatively low-mass galaxies ($\sim 10^{10}\ M_{\odot}$) are well separated from each other. The *Spitzer* observations were carried out for the two components separately, and the final maps are co-adds of these separate observations. Both components are well detected by IRAC and MIPS, and both show extended IR emission throughout the entire disks. There is a strong outer disk starburst on the east side of the eastern component (NGC 3023), whose FIR luminosity is comparable to that of the nucleus.

J1020+4831. The eastern component (E type) is a strong radio source (4C +48.29), classified as an AGN in the literature according to NED. It is a rather weak FIR source, only marginally detected in the 24 μm band, and undetected in the 70 and 160 μm bands. The western component (S type), detected in all seven *Spitzer* bands, dominates the dust emission of the pair.

J1027+0114. This close S+E pair is actually in a triplet (Karachentseva et al. 1988). The third galaxy, west of the pair, is about 2′ away from the pair center. The southern component (S type) is a strong IR source. The northern component (E type) is detected marginally by MIPS in the 24 μm band.

J1043+0645. Both components of this S+S pair are detected by IRAC and MIPS. The two components have nearly equal

mass (the mass ratio derived from the *K*-band luminosities is $M_1/M_2 = 1.2$), but rather uneven dust emissions. The $L_{\rm TIR}$ of the western component is more than 5 times of that of the eastern component.

J1051+5101. This is KPG 253, which appears to be a very close S+E pair. The projected separation of the two components ($s = 4.7\ h^{-1}$ kpc) is actually less than the $5\ h^{-1}$ kpc lower boundary of the separation criterion. However, since the separation is only 6% off the boundary, we chose to keep the pair in this work. It is in the center of a cluster. Both galaxies are massive ($> 10^{11}\ M_\odot$). The western galaxy is classified as E while the eastern galaxy as S. At low surface brightness levels, a ring-like structure shows up around the nucleus of the S component both in the optical and in the 8 μm images. The pair is detected by *IRAS* with $f_{60} = 0.78$ Jy. Interestingly, both the 24 μm and 70 μm band emission contours coincide with the nucleus of the E component while there is little emission detected in the nuclear region of the S component. This indicates that most of the star formation in the pair is occurring in the nucleus of the more massive E component, perhaps due to an interstellar medium transfer from the S component. The total SFR derived from the IR emission is quite low, at the level of $\sim 1\ M_\odot\ {\rm yr}^{-1}$, very different from IR-selected mergers. No AGN or any detectable radio source has been found in the pair (van Driel et al. 2000).

J1202+5342. The western component (S type) dominates the dust emission the S+E pair.

J1308+0422 = UGC 8217. Both galaxies in this S+S pair are well detected in all seven *Spitzer* bands with nearly equal $L_{\rm TIR}$ ($\simeq 4\ \times 10^9\ L_\odot$).

J1332−0301. Both spiral galaxies are detected by IRAC and MIPS. The western component, with the lower mass and more compact morphology among the two, has warmer (i.e., higher f_{70}/f_{160} ratio) and stronger dust emission than the eastern component.

J1346−0325. The two galaxies of this S+E pair are well separated from each other. Both are detected by IRAC and MIPS, with comparable, moderate dust emission. The eastern component (an E type) has an Sy2 nucleus (Maia et al. 2003).

J1400+4251. This S+S pair is a bright *IRAS* source ($f_{60} = 2.32$ Jy). The combined $L_{\rm TIR}$ ($= 1.3 \times 10^{11}\ L_\odot$) makes the pair a LIRG. The two spiral galaxies, both detected by IRAC and MIPS, are about equally bright in the dust emission. When separated, each is slightly fainter than a LIRG.

J1425+0313. This S+E pair is VIII Zw 415. The western component (E type), a moderate IR source, contains a broad-line AGN (Hao et al. 2005).

J1433+4004 = KPG 426. These are two IR bright spiral galaxies, both are detected by IRAC and MIPS. There are bright hot spots in the 8 μm image of the southern galaxy. As a close-interacting S+S pair, it has been studied by Xu et al. (2001) using ISOCAM.

J1453+0317. One of the three pairs in our sample that are larger than 2.′5. These are two well-separated S-type galaxies, both are detected by IRAC and MIPS. The eastern galaxy displays a ring formation in both 8 and 24 μm images. The western galaxy was detected in the ISOPHOT 170 micron Serendipity Survey (Stickel et al. 2004), with $f_{170} = 1.94 \pm 0.58$ Jy. This is significantly lower than the MIPS 160 μm flux: $f_{160} = 3.03 \pm 0.32$ Jy.

J1506+0346. An S+S pair. The western component (IC 1087), classified as S0-a (via NED), is a weak IR source. Most of the dust emission is from the eastern component (UGC 09710).

J1510+5810. These are two very close S-types. The source about 1′ west of the pair is a star. Most of the dust emission is due to the eastern component. It was detected in the ISOPHOT 170 micron Serendipity Survey (Stickel et al. 2004), with $f_{170} = 0.87 \pm 0.26$ Jy. This is slightly lower than the MIPS 160 μm flux: $f_{160} = 1.16 \pm 0.12$ Jy.

J1528+4255 = I Zw 113. These two spiral galaxies show signs of interaction. Most of the dust emission is found in the western component (NGC 5934).

J1556+4757. The western component (S type) dominates the dust emission in the S+E pair. The source between the two galaxies is a star.

1602+4111 = KPG 479. Both spiral galaxies are IR bright. They show signs of interactions.

1704+3448. These are two closely interacting, star-forming spiral galaxies. The northern component is a LIRG.

J2047+0019 = KPG 548. The S+E pair is one of the three pairs in the KPAIR sample with size $> 2.'5$. The western component (S type), well resolved in both the IRAC and the MIPS bands, shows a nucleus+ring structure. In the MIPS bands, the ring is rather faint. The eastern component (E type) is only marginally detected in the 24 μm band, undetected in the 70 and 160 μm bands. This pair has been studied by Domingue et al. (2003) with ISOPHOT.

J1315+6207 = UGC08335 = Arp 238 = KPG 369 = VV 250. This S+S pair is not displayed in Figure 1. It was observed successfully by J. M. Mazzarella et al. (2010, in preparation) in the IRAC bands, but the MIPS observations failed. The IRAC images (J. M. Mazzarella et al. 2010, in preparation) and the KAO image at 100 μm (Bushouse et al. 1998) show that the eastern component dominates the IR emission of this LIRG pair. The west component was undetected in the KAO observation (Bushouse et al. 1998). The radio continuum observations at 4.85 GHz (Condon et al. 1991) revealed a flux ratio between the two components of 4.4 (22 mJy/5 mJy), close to the 8 μm flux ratio of 3.5 (187 mJy/54 mJy) measured by J. M. Mazzarella et al. (2010, in preparation). Compared to the *IRAS* data, Condon et al. (1991) found an FIR/radio ratio index $q = 2.74$ for the pair, very close to the mean ($\langle q \rangle = 2.64 \pm 0.16$) for star-forming galaxies. Assuming that both components have the same FIR/radio ratio (e.g., Hattori et al. 2004), we divided the total IR luminosity of the pair, $\log(L_{\rm TIR}/L_\odot) = 11.74$ (J. M. Mazzarella et al. 2010, in preparation), and found $\log(L_{\rm TIR}/L_\odot) = 11.65$ for the east component and $\log(L_{\rm TIR}/L_\odot) = 11.01$ for the west component. Therefore, both galaxies qualify as LIRGs.

APPENDIX B

MIPS POINT RESPONSE FUNCTIONS (PRFs)

The 24 μm PRF was taken from Engelbracht et al. (2007). It was generated by smoothing the standard Spitzer TinyTim PSF (Krist 1993) with a 4.″41 ("1.8 pixel") boxcar. Similarly, the 70 μm PRF was taken from Gordon et al. (2007), which is a TinyTim PSF smoothed by a 13.″30 ("1.35 pixel") boxcar. As shown in Figure A.1, good agreements were found between our data and the above model PRFs.

On the other hand, the comparison between our data in the 160 μm band and the standard PRF ("STinyTim+1.6-pixel boxcar") of the MIPS team (Stansberry et al. 2007) showed an excess in the first Airy ring in our data (Figure A.2). In order to better fit the data, we adopted an empirical PRF. It is the standard PRF plus a ring, which has a truncated Gaussian

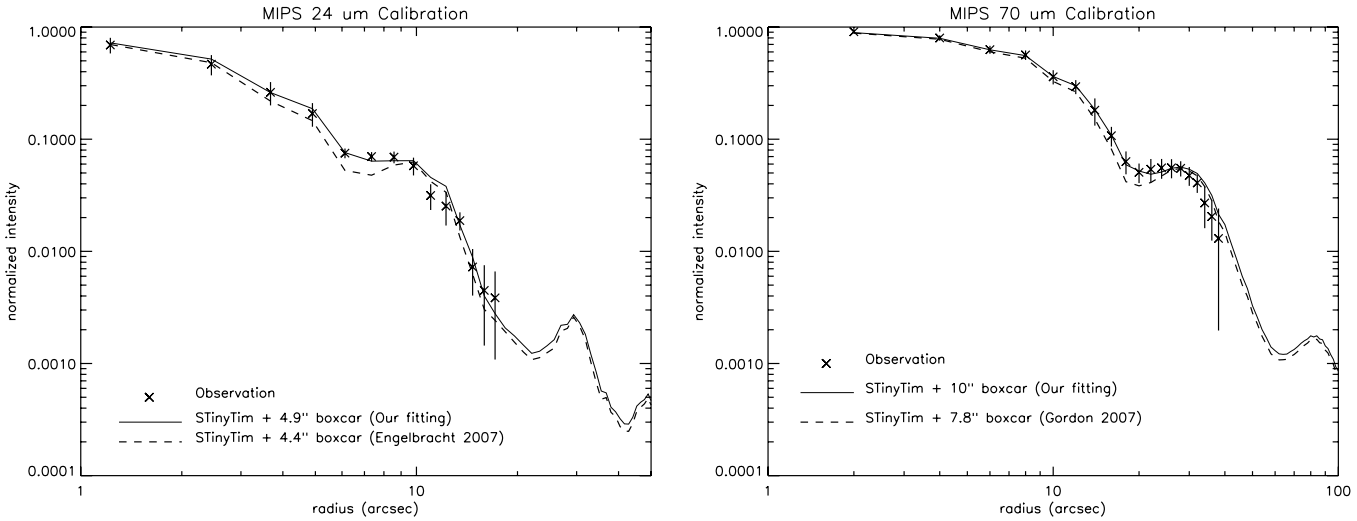

Figure A1. Left: the 24 μm point response functions (PRFs). Right: the 70 μm PRFs.

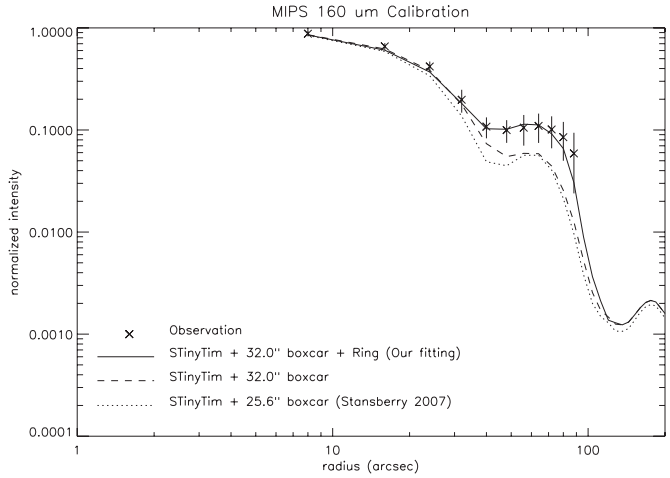

Figure A2. 160 μm PRFs.

profile:

$$S = S_1 \times \exp \frac{(r - r_1)^2}{2\sigma_1^2} \quad (r \leqslant r_2) \tag{B1}$$

$$= 0 \quad (r > r_2); \tag{B2}$$

where $S_1 = 0.05$, $r_1 = 5$ pixel, $r_2 = 8$ pixel, and $\sigma_1 = 4$ pixel. The pixel size is $8''$ for the 160 μm map. The comparisons between 160 μm PRFs and the data can be found in Figure A.2.

REFERENCES

Abazajian, K., et al. 2005, AJ, 129, 1755
Abraham, R., et al. 1996, MNRAS, 279, L47
Alonso, M. S., et al. 2004, MNRAS, 352, 1081
Appleton, P. N., et al. 2003, ApJ, 586, 112
Barnes, J., & Hernquist, L. 1996, ApJ, 471, 115
Barton, E. J., Geller, M. J., & Kenyon, S. J. 2000, ApJ, 530, 660
Barton, E. J., et al. 2007, ApJ, 671, 1538
Bell, E., & De Jong, R. S. 2001, ApJ, 550, 212
Bell, E. F., et al. 2005, ApJ, 625, 23
Bergvall, N., Laurikainen, E., & Aalto, S. 2003, A&A, 405, 31
Berrier, J. C., et al. 2006, ApJ, 652, 56
Boselli, A., & Gavazzi, G. 2006, PASP, 118, 517
Bridge, C. R., et al. 2007, ApJ, 659, 931
Brinchmann, J., et al. 1998, ApJ, 499, 112
Brinchmann, J., et al. 2004, MNRAS, 351, 1151
Brosch, N., Almoznino, E., & Heller, A. B. 2004, MNRAS, 349, 357
Buat, V., & Xu, C. 1996, A&A, 306, 61
Bundy, K., et al. 2004, ApJ, 601, L123
Burkey, J. M., et al. 1994, ApJ, 429, L13
Bushouse, H., Telesco, C. M., & Werner, M. W. 1998, AJ, 115, 938
Calzetti, D., et al. 2005, ApJ, 633, 871
Carlberg, R. G., Pritchet, C. J., & Infante, L. 1994, ApJ, 435, 540
Carlberg, R. G., et al. 2000, ApJ, 532, L1
Cole, S., et al. 2001, MNRAS, 326, 255
Condon, J. J., Frayer, D. T., & Broderick, J. J. 1991, AJ, 101, 362
Conselice, C. J. 2006, ApJ, 638, 686
Conselice, C. J., Bershady, M. A., Dickinson, M., & Papovich, C. 2003, AJ, 126, 1183
Dale, D. A., & Helou, G. 2002, ApJ, 576, 159
Dale, D. A., et al. 2005, ApJ, 633, 857
De Vaucouleurs, G., De Vaucouleurs, A., & Corwin, H. G. 1976, Second Reference Catalogue of Bright Galaxies (Austin, TX: Univ. Texas Press)
Di Matteo, P., Bournaud, F., Martig, M., Combes, F., Melchior, A.-L., & Semelin, B. 2008, A&A, 492, 31
Domingue, D. L., Xu, C. K., Jarrett, T. H., & Cheng, Y.-W. 2009, ApJ, 695, 1559
Domingue, D. L., et al. 2003, AJ, 125, 555
Driver, S., et al. 1995, ApJ, 449, L23
Duc, P.-A., Brinks, E., Wink, J. E., & Mirabel, I. F. 1997, A&A, 326, 537
Elbaz, D., Cesarsky, C. J., Chanial, P., Franceschini, A., Fadda, D., & Chary, R. R. 2002, A&A, 384, 848
Ellison, S., Patton, D. R., Simard, L., & McConnachie, A. W. 2008, AJ, 135, 1877
Engelbracht, C. W., et al. 2007, PASP, 119, 994
Fazio, G. G., et al. 2004, ApJS, 154, 10
Flores, H., et al. 1999, ApJ, 517, 148
Gao, Y., & Solomon, P. M. 1999, ApJ, 512, 99
Glazebrook, K., Ellis, R., Santiago, B., & Griffiths, R. 1995, MNRAS, 275, L19
Gordon, C. D., et al. 2007, PASP, 119, 1019
Grützbauch, R., et al. 2007, AJ, 133, 220
Guo, Q., & White, S. D. M. 2008, MNRAS, 384, 2
Hammer, F., et al. 2005, A&A, 430, 115
Hao, L., et al. 2005, AJ, 129, 1783
Hattori, T., et al. 2004, AJ, 127, 736
Hernández-Toledo, M. H., & Puerari, I. 2001, A&A, 379, 54
Hernquist, L., & Barnes, J. 1991, Nature, 354, 210
Hopkins, A. M. 2004, ApJ, 615, 209
Iglesias-Paramo, J., et al. 2004, A&A, 419, 109
Jarrett, T. H., Chester, T., & Cutri, R. 2000, AJ, 119, 2498
Jogee, S., et al. 2009, ApJ, 697, 1971
Joseph, R. D., Meikle, W. P. S., Robertson, N. A., & Wright, G. S. 1984, MNRAS, 209, 111

Kampczyk, P., et al. 2007, ApJS, 172, 329
Karachentsev, I. 1972, Comm. Spec. Ap. Obs. USSR, 7, 1
Karachentseva, V. E., Karachentsev, I. D., & Lebedev, V. S. 1988, Astrofizik. Issledovanija, Special Obs., 26, 42
Kartaltepe, J. S., et al. 2007, ApJS, 172, 320
Kauffmann, G., et al. 2003, MNRAS, 341, 33
Kauffmann, G., et al. 2004, MNRAS, 353, 713
Kennicutt, R. C., Jr. 1998, ARA&A, 36, 189
Kennicutt, R. C., Jr., et al. 1987, AJ, 93, 1001
Kennicutt, R. C., Jr., et al. 2003, PASP, 115, 928
Keres, D., et al. 2009, MNRAS, 309, 160
Khochfar, S., & Burkert, A. 2001, ApJ, 561, 517
Kitzbichler, M. G., & White, S. D. M. 2008, MNRAS, 391, 1489
Kochanek, C. S., et al. 2001, ApJ, 560, 566
Krist, J. 1993, in ASP Conf. Ser. 52, Astronomical Data Analysis Software and Systems II, ed. R. J. Hanisch, R. J. V. Brissenden, & Jeannette Barnes (San Francisco, CA: ASP), 536
Lacey, C., & Cole, S. 1993, MNRAS, 262, 627
Lambas, D. G., Tissera, P. B., Alonso, M. S., & Coldwell, G. 2003, MNRAS, 346, 1189
Lavery, R. J., et al. 2004, ApJ, 612, 679
Le Févre, O., et al. 2000, MNRAS, 311, 565
Le Flóch, E., et al. 2005, ApJ, 632, 169
Li, C., et al. 2008, MNRAS, 385, 1903
Lilly, S. J., Le Févre, O., Hammer, F., & Crampton, D. 1996, ApJ, 460, L1
Lin, L., Patton, D. R., & Koo, D. C. 2008, ApJ, 681, 232
Lin, L., et al. 2004, ApJ, 617, L9
Lonsdale, C. J., et al. 2003, PASP, 115, 897
Lotz, J. M., et al. 2008, ApJ, 672, 177
Madau, P., Pozzetti, L., & Dickinson, M. 1998, ApJ, 498, 106
Maia, M. A. G., Machado, R. S., & Willmer, C. N. A. 2003, AJ, 126, 175
Maller, A. H., et al. 2006, ApJ, 674, 763
Marchesini, D., et al. 2007, ApJ, 665, 42
Melbourne, J., Koo, D. C., & Le Flóch, E. 2005, ApJ, 632, L65
Mihos, J. C., McGaugh, S. S., & de Blok, W. J. G. 1997, ApJ, 477, L79
Moshir, M., Kopman, G., & Conrow, T. A. O. 1992, IRAS Faint Source Catalogue, Version 2 (Pasadena, CA: California Institute of Technology)
Nikolic, B., Cullen, H., & Alexander, P. 2004, MNRAS, 355, 874
Park, C., & Choi, Y.-Y. 2005, ApJ, 635, L29
Park, C., & Choi, Y.-Y. 2009, ApJ, 635, L29
Patton, D. R., et al. 1997, ApJ, 475, 29
Patton, D. R., et al. 2002, ApJ, 565, 208
Rasmussen, J., et al. 2008, MNRAS, 388, 1245
Rieke, G. H., et al. 2004, ApJS, 154, 25
Sanders, D. B., & Mirabel, I. F. 1996, ARA&A, 34, 749
Schiminovich, D., et al. 2007, ApJS, 173, 315
Shupe, D. L., et al. 2008, AJ, 135, 1050
Smith, B. J., et al. 2007, AJ, 133, 791
Stansberry, J. A., et al. 2007, PASP, 119, 1038
Stickel, M., Lemke, D., Klaas, U., Krause, O., & Egner, S. 2004, A&A, 422, 39
Sulentic, J. W. 1989, AJ, 98, 2066
Surace, J. A., et al. 2005, SWIRE Data Release 2 Document, (Pasadena, CA: Caltech), http://data.spitzer.caltech.edu/popular/swire/20050603_enhanced/documentation/SWIRE2_doc_083105.pdf
Telesco, C., Wolstencroft, R. R., & Done, C. 1988, ApJ, 329, 174
Telles, E., & Maddox, S. 2000, MNRAS, 311, 307
Toomre, A. 1977, in The Evolution of Galaxies and Stellar Populations, ed. B. M. Tinsley & R. B. Larson (New Haven, CT: Yale Univ. Press), 401
van Driel, W., Arnaboldi, M., Combes, F., & Sparke, L. S. 2000, A&AS, 141, 385
Verdes-Montenegro, L., et al. 2001, A&A, 377, 812
Wolf, C., Meisenheimer, K., Rix, H.-W., Borch, A., Dye, S., & Kleinheinrich, M. 2003, A&A, 401, 73
Woods, D., Fahlman, G. G., & Richer, H. B. 1995, ApJ, 454, 32
Woods, D. F., & Geller, M. J. 2007, AJ, 134, 527
Woods, D. F., Geller, M. J., & Barton, E. J. 2006, AJ, 132, 197
Wu, W., & Keel, W. C. 1998, AJ, 116, 1513
Xu, C., & Sulentic, J. W. 1991, ApJ, 374, 407
Xu, C. K., Sun, Y. C., & He, X. T. 2004, ApJ, 603, 73L
Xu, C., et al. 2001, ApJ, 541, 644
Yee, H. K. C., & Ellingson, E. 1995, ApJ, 445, 37
Yun, M. S., Reddy, N. A., & Condon, J. J. 2001, ApJ, 554, 803
Zepf, S. E., & Koo, D. C. 1989, ApJ, 337, 34
Zheng, X. Z., et al. 2004, A&A, 421, 847
Zheng, X. Z., et al. 2007, ApJ, 661, L47